

1 **Mouse retinal cell behaviour in space and time using light sheet fluorescence**  
2 **microscopy**

3  
4 Claudia Prahst\*<sup>1#</sup>, Parham Ashrafzadeh<sup>2#</sup>, Kyle Harrington<sup>1,π</sup>, Lakshmi Venkatraman<sup>1,2</sup>, Mark  
5 Richards<sup>2</sup>, Ana Martins Russo<sup>3</sup>, Kin-Sang Cho<sup>4,5</sup>, Karen Chang<sup>4</sup>, Thomas Mead<sup>8</sup>, Dong Feng  
6 Chen<sup>4</sup>, Douglas Richardson<sup>6</sup>, Lena Claesson-Welsh<sup>2</sup>, Claudio Franco<sup>3</sup>, Katie Bentley\*<sup>1,2,7,8,9</sup>

7 <sup>1</sup> Center for Vascular Biology Research and Department of Pathology, Beth Israel Deaconess  
8 Medical Center and Harvard Medical School, Boston, MA 02215, USA.

9 <sup>2</sup> The Beijer Laboratory, Department of Immunology, Genetics and Pathology, Uppsala  
10 University, Uppsala, Sweden.

11 <sup>3</sup> Instituto de Medicina Molecular, Lisbon, Portugal

12 <sup>4</sup> Schepens Eye Research Institute of Massachusetts Eye and Ear, Department of  
13 Ophthalmology, Harvard Medical School, Boston, MA 02114, USA.

14 <sup>5</sup> Geriatric Research Education and Clinical Center, Office of Research and Development, Edith  
15 Nourse Rogers Memorial Veterans Hospital, Bedford, MA 01730, USA.

16 <sup>6</sup> Harvard Center for Biological Imaging, Department of Molecular and Cellular Biology, Harvard  
17 University, Cambridge, MA 02138, USA.

18 <sup>7</sup> Biomedical Engineering Department, Boston University, Boston, MA 02215 USA

19 <sup>8</sup> The Francis Crick Institute, 1 Midland Road, London UK

20 <sup>9</sup> Department of Informatics, Faculty of Natural and Mathematical sciences, Kings College  
21 London, UK

22 <sup>π</sup>Current address: Virtual Technology and Design, University of Idaho, Moscow, ID 83844, USA.

23 <sup>#</sup> Contributed equally to this work.

24 \*Corresponding authors

25 [Katie.bentley@kcl.ac.uk](mailto:Katie.bentley@kcl.ac.uk) / [katieab@bu.edu](mailto:katieab@bu.edu)

26 [Claudia.prahst@gmail.com](mailto:Claudia.prahst@gmail.com)



28 **Abstract**

29 As the general population ages and the incidence of diabetes increases epidemically, more  
30 people are affected by eye diseases, such as retinopathies. It is therefore critical to improve  
31 imaging of eye disease mouse models. Here, we demonstrate that 1) rapid, quantitative 3D and  
32 4D (time lapse) imaging of cellular and subcellular processes in the murine eye is feasible, with  
33 and without tissue clearing, using light-sheet fluorescent microscopy (LSFM) and 2) LSFM  
34 readily reveals new features of even well studied eye disease mouse models, such as the  
35 Oxygen-Induced Retinopathy (OIR) model. Through correlative LSFM-Confocal imaging we find  
36 that flat-mounting retinas for confocal microscopy significantly distorts tissue morphology. The  
37 minimized distortion with LSFM dramatically improved analysis of pathological vascular tufts in  
38 the OIR model revealing “knotted” morphologies, leading to a proposed new tuft nomenclature.  
39 Furthermore, live-imaging of OIR tuft formation revealed abnormal cell motility and altered  
40 filopodia dynamics. We conclude that quantitative 3D/4D LSFM imaging and analysis has the  
41 potential to advance our understanding of pathological processes in the eye, in particular neuro-  
42 vascular degenerative processes.

43

44

45

46

47

48

49

50

51

52

53

## 54 **Introduction**

55           Eye diseases, such as diabetic retinopathy, age-related macular degeneration, cataract,  
56 and glaucoma are becoming increasingly common with the increased age of the general  
57 population. Although advances in understanding and treating eye diseases have been made,  
58 the molecular mechanisms involved are still not fully understood. We believe that is partially due  
59 to the inadequate ability to image eye tissue in its natural, spherical state, to reveal the many  
60 distinct layers with interacting cell types oriented differentially within or between the layers.  
61 Optical Coherence Tomography (OCT) is an established medical imaging technique that uses  
62 light to capture micrometer-resolution, three-dimensional images non-invasively, now widely  
63 used as a diagnostic tool (Srinivasan et al. 2006; Huber et al. 2009). Its main strength lies in  
64 revealing information on tissue depth preserving the eyes natural state. However, its limitation  
65 lies in not being able to provide a wide field of view, cellular or molecular information.  
66 Furthermore, being a non-fluorescent method, specific proteins cannot be labelled and tracked  
67 to investigate mechanism. Currently only confocal microscopy can deliver this detailed  
68 fluorescently labelled information (Del Toro et al. 2010), but the 3D nature of the tissue is likely  
69 distorted during flat-mounting and it is currently not known to what extent this might impact the  
70 obtained results. For instance, the vascular biology field is one clear example where these  
71 limitations can have a substantial impact. The mouse retina is a common model used to study  
72 vascular development and disease; confocal imaging approaches have been used to measure  
73 vessel morphology, vascular malformations, junctional organization, and pathological tuft  
74 formation (Gerhardt et al. 2003; Bentley et al. 2014; Stahl et al. 2010). Moreover, vessel  
75 diameters are now being used to predict blood flow (Bernabeu et al. 2014, Baeyens et al.,  
76 2016). Distortions arising from confocal flat-mounting could therefore have important  
77 ramifications for the overall conclusions of several studies.

78           Changes in cellular and tissue morphology are a hallmark of many eye diseases. For  
79 instance, retinopathy of prematurity and diabetic retinopathy are characterized by excessive,

80 bulbous and leaky blood vessels that protrude out of their usual layered locations. These  
81 malformed vessels cause many problems including the generation of abnormal mechanical  
82 traction, which pulls on the different layers, eventually leading to detachment of the retina  
83 (Nentwich & Ulbig 2015; Hartnett 2015). Yet, very limited information has arisen on the  
84 conformation and morphogenesis mechanisms of these vascular tuft malformations, despite a  
85 wealth of confocal studies of the related Oxygen Induced Retinopathy (OIR) mouse model  
86 (Connor et al. 2009).

87 Another limitation of confocal microscopy for imaging of mouse retinal angiogenesis is  
88 the inability to perform live imaging of endothelial cell dynamics. Endothelial cells move and  
89 connect in highly dynamic, complex ways to generate the extensive vascular networks required  
90 to perfuse the retina over time (angiogenesis). Whilst live-imaging techniques of blood vessels  
91 exist, such as the dorsal skinfold chamber or the cranial window (Brown et al. 2010), it is not  
92 possible to translate those to study retinal angiogenesis, as the mouse pups are very small,  
93 making it hard to access the retina tissue. There are a small number of reports on *ex vivo* live-  
94 imaging of the retinal vasculature with confocal microscopy, but with limited success as  
95 flatmounting the retina for live-imaging takes time from dissection to culture, and it is necessary  
96 to physically force the tissue onto the membrane, disturbing local tissue arrangement and  
97 mechanics (Sawamiphak et al. 2010, Rezzola et al. 2013). Furthermore, photobleaching,  
98 phototoxicity and long acquisition times continue to remain an issue.

99 Recent advances in Light Sheet Fluorescence Microscopy (LSFM) have demonstrated  
100 its strength for allowing the rapid acquisition of optical sections through thick tissue samples  
101 such as mouse brains (Stelzer 2014). Instead of illuminating or scanning the whole sample  
102 through the imaging objective, as in wide-field or confocal microscopy, the sample is illuminated  
103 from the side with a thin sheet of light. Thus, in principle LSFM would require little interference  
104 with the original spherical eye tissue structure, avoiding distortion of the tissue with flat-  
105 mounting. Moreover, LSFM is becoming a gold-standard technique to perform live-imaging in

106 whole organs/organisms because it permits imaging of thick tissue sections without disturbing  
107 the local environment, while also reducing photobleaching and phototoxicity (Stelzer 2014;  
108 Reynaud et al. 2014). Thus, here we investigate the feasibility, advantages and disadvantages  
109 of LSFM for imaging the mouse eye for development or disease studies. We present an  
110 optimized LSFM protocol to rapidly image neurovascular structures, across scales from the  
111 entire eye to subcellular components in mouse retinas. We investigate the pros and cons of  
112 LSFM imaging of vessels over standard confocal imaging techniques in early mouse pup  
113 retinas. Importantly, we also demonstrate the benefits of LSFM using the OIR mouse model,  
114 where we discover previously unappreciated new spatial arrangements of endothelial cells in  
115 the onset of vascular tuft malformations due to the improved undistorted, 3D and 4D imaging  
116 capabilities of LSFM.

117 We conclude that LSFM quantitative 3D/4D imaging and analysis has the potential to  
118 advance our understanding of healthy and pathological processes in the eye, with a particular  
119 relevance for the vascular and neurovascular biology fields, as well as Ophthalmology.

120

121 **Results**

122 **LSFM enables rapid 3D imaging of mouse eyes, and in particular retinas, in their natural**  
123 **state**

124 To visualize the retinal vasculature using epifluorescence or confocal microscopes, the retina is  
125 flat-mounted by making four incisions before adding a cover slip containing mounting medium  
126 onto glass slides (Fig. 1a, upper panel). To image samples using LSFM, however, samples are  
127 suspended in their natural state in low-melting agarose (Fig. 1a, lower panel). This enables  
128 imaging of the vasculature of large and intact samples such as the whole eyeball (minus the  
129 sclera and cornea) (Fig. 1b), the iris (Fig. 1c), or the optic nerve (Fig. 1d). Using LSFM, it was  
130 possible to observe the superficial, intermediate and deep vascular plexus (Fig. 1e and Suppl.  
131 Fig. 1b) of a retina in its native conformation (Fig. 1f). In contrast to imaging the retinal  
132 vasculature using the confocal microscope, where stacks contain 8 - 15 images, acquiring a  
133 stack of the retina using LSFM contains 200 - 300 images, but the imaging time is much shorter  
134 (~60 sec vs. ~10 min).

135 Imaging the iris microvasculature (Fig. 1c) surprisingly revealed that the vasculature  
136 network is immature at P15 (Fig. 1b, Suppl. Fig. 1), and that it remodels into a mature network  
137 in adulthood (Fig. 1c). A network of capillaries was visible at P15, whereas the adult  
138 microvasculature consisted of radial branches of small vessels and capillaries in a relatively  
139 linear pattern. The major arterial circles (MICs) around the iris root were developed in both P15  
140 and adult mice (Fig. 1c and Suppl. Fig. 1a, yellow arrows). The images generated from adult  
141 mice using LSFM are consistent with a previous report using OCT to image the iris  
142 microvasculature (Choi et al. 2014). Using LSFM, the vessels appeared straighter, and the  
143 MICs were not as close to the iris root, which could be because OCT involves live-imaging of  
144 the vasculature, without mechanically removing the sclera and cornea.

145 We next tested whether LSFM could resolve subcellular structures in the retinal  
146 vasculature such as the Golgi apparatus, which has recently been shown to be important for

147 inferring cell polarity during vessel regression (Franco, C.A. et al. 2015). We found it feasible to  
148 stain and image the Golgi organelle (Golp4, Alexa 647) and the collagen IV-containing  
149 basement membrane around the vessels (Suppl. Fig. 1c, d). On static images of mice  
150 expressing lifeAct-enhanced green fluorescent protein (EGFP) we performed deconvolution to  
151 reduce the light scattering effects and found this gave a marked improvement to the resolution  
152 of actin bundles within endothelial cells (Suppl. Fig. 1e-i). Taken together, LSFM can rapidly  
153 generate 3D images of the murine eye in its native form across scales, with tissue, cellular and  
154 subcellular resolution.

155

### 156 **LSFM enables concurrent imaging of retinal cell types within and between the retinal** 157 **layers**

158 A growing number of reports show that neurovascular interactions in the eye are important  
159 during development and disease progression (Akula et al. 2007; Narayanan et al., 2014;  
160 Nentwich and Ulbig, 2015; Usui et al. 2015; Verheyen et al. 2012). Neurons and vessels are  
161 however currently difficult to image in the same retinal tissue across all layers, without distortion  
162 due to the way they are arranged in the retina (Fig. 2a, b). Neurons are currently imaged by  
163 making vertical sections, orthogonal to the three vascular layers (the superficial, intermediate  
164 and deep plexus) (Fig. 2b “side view”), on paraffin or cryo-embedded retinas, which necessarily  
165 means losing the ability to observe vascular branching in the horizontal layer in the same tissue.  
166 Likewise, studies focused on the retinal vasculature use whole mount images of the retina  
167 viewed from above (Fig. 2b, “top view”) using horizontal optical sections (Usui et al. 2015),  
168 which does not allow proper imaging of retinal neurons spanning between the layers because of  
169 insufficient z-resolution in confocal microscopy. Thus, we next investigated whether concurrent  
170 imaging of neurons and vessels in the same sample might be achieved with the optical  
171 sectioning and rotational viewing capacity of LSFM.



172 We found that eye cups from P3 C57BL/6 Thy1-YFP mice, labelling retinal ganglion cells  
173 in yellow combined with IsolectinB4 labeled vasculature provided 3D high resolution images  
174 without the need for tissue clearing (Fig. 2c, d, Movie S1). However, we found that including  
175 lipid removal/permeabilization as part of a full tissue clearing protocol further improves  
176 resolution for eye cups at later stages of development, when more of the retinal layers have  
177 formed (Fig. 2e-h), as it decreases the scattered light caused by imaging thicker tissue with the  
178 light sheet (Richardson & Lichtman 2015).

179 We tested several different clearing methods to see which was better suited to retinal  
180 tissue. We first tested the aqueous-based clearing methods ScaleA2 and FRUIT (Hou et al.  
181 2015; Hama et al. 2011). However, these clearing methods did not lead to higher quality images  
182 and made tissue-handling very difficult during imaging due to the high viscosity of the FRUIT  
183 clearing agent. We also tested the passive aqueous-based methods CUBIC-R (Kubota et al.  
184 2017) and PROTOS (Murray et al. 2015), but again found little improvement. Since many  
185 studies use animals genetically engineered to express fluorescent markers such as Tomato or  
186 GFP, we decided not pursue solvent-based clearing methods such as iDISCO, which do not  
187 maintain fluorescent protein emission for more than a few days after the clearing process  
188 (Renier et al. 2014). Overall, we found PACT was the most efficient and effective clearing  
189 method for retinal tissue, likely because it is relatively thin (Yang et al. 2014; Treweek et al.  
190 2015a). PACT cleared adult retinas with Draq5 staining, which stains all nuclei, visualizing the  
191 inner nuclear layer (INL) and outer nuclear layer (ONL) (Fig. 2f, Movie S2). The deep vascular  
192 plexus, visualized by IsolectinB4 staining could be seen between the ONL and INL, whereas the  
193 intermediate vascular plexus bordered the INL as expected. The superficial vascular plexus is  
194 located on the inner retinal surface together with nuclei of the retinal ganglion cells (Fig, 2f,  
195 Movie S2). Adult retinas were co-immunostained for Tuj1 and Calbindin, markers for retinal  
196 ganglion cells and horizontal cells, respectively. This immunostaining made it possible to  
197 appreciate the distance between these two cell types in the fully developed retina (Fig. 2g,

198 Movie S3). 3D-rendered images of co-staining for smooth muscle actin and collagenIV  
199 moreover showed arteries of the superficial vascular plexus covered with smooth muscle cells  
200 (Fig. 2h, Movie S4).

201

## 202 **Vessel distortion due to confocal flatmounting revealed by correlative LSFM-Confocal** 203 **imaging**

204 As vascular measurements taken from confocal images are used as the standard for  
205 inferring the actual sizes of vascular structures in the retina, we next aimed to systematically  
206 quantify the 3D distortion of vascular structures incurred by flat-mounting and confocal imaging.  
207 In order to make direct, quantitative comparisons of the relatively small vessels in the superficial  
208 plexus, we used a correlative LSFM-Confocal approach: we first imaged the retinal tissue with  
209 LSFM, which retains the natural tissue curvature, then we melted the gel and flat-mounted the  
210 same retina onto a coverslip and imaged it again using confocal microscopy (Fig 3a). We first  
211 analyzed the largest vessels near the optic nerve and then smaller capillaries in the sprouting  
212 vascular front from P4 wt retinas. Images obtained with our correlative LSFM-confocal approach  
213 were then brightness/contrast adjusted and cropped and surface rendered using Imaris to focus  
214 on small regions of same vessel segments in the corresponding confocal and LSFM images.  
215 Dramatically shallower side views and cross-sections of vessels were evident in the confocal  
216 images compared to LSFM (Fig. 3b). We next quantified this shift in aspect ratio by measuring  
217 the diameter taken across the vessel in XY (hereafter “Width”) and down through the Z-axis  
218 (hereafter “Depth”) in confocal (Fig. 3c). For LSFM images, given the tissue can be at any  
219 orientation in the agarose with respect to the objective, the XYZ coordinate system of the image  
220 stack is not indicative of the equivalent width/depth measurement in confocal. Therefore, the  
221 orientation of the surrounding vascular plexus at the point of the vessel segment was used as a  
222 reference surface “plexus plane” to make the corresponding “width” diameter measurement, as  
223 it is equivalent to the XY plane in the corresponding confocal image. Similarly, the “depth”

224 diameter in LSFM was defined as perpendicular to the plexus plane and width measurement  
225 (equivalent to the diameter through the z-stack in confocal). Vessels were significantly more  
226 elliptical (wider and shallower) under confocal than LSFM indicative of being compressed during  
227 flat-mounting (Fig. 3d,e).

228

229 **LSFM enables 4D live-imaging with subcellular resolution, revealing rapid, transient “kiss**  
230 **and run” tip cell adhesions at the sprouting front.**

231 *Ex vivo* live-imaging could be a useful tool to study tip cell guidance during the angiogenic  
232 sprouting process in the mouse retina, but it has proven to be challenging with conventional  
233 microscopy. Existing *ex vivo* confocal methods to live-image retinal vasculature, tissue handling  
234 leads to damage of the tissue, as it involves either flat-mounting the retinas onto a membrane  
235 and then submerging it in medium (Sawamiphak et al. 2010), or cutting the retina into fragments  
236 and embedding them in fibrin gels prior to imaging (Rezzola et al. 2013).

237 We therefore established a protocol for live-imaging of the growing retinal vasculature  
238 using LSFM. We first crossed mT/mG mice with Cdh5(PAC)-CreERT2 mice and injected them  
239 with tamoxifen to induce endothelial GFP expression (Muzumdar et al. 2007; 2010; Wang et al.  
240 2010). Surprisingly, connections between ECs formed very rapidly (within 20 min) and  
241 regressed just as rapidly (Fig. 4a, Movie S5). Such transient “kiss and run” adhesion and  
242 release style interactions between ECs (as opposed to full adhesions or anastomoses, where  
243 the connections stably remain) have only been previously reported in glycolysis-deficient ECs *in*  
244 *vitro* with “normal” connections being more stable *in vitro* (Schoors et al. 2014). The dynamics *in*  
245 *vivo* were therefore assumed to be slower and more stable than *in vitro* live-imaging, however  
246 our new observations indicate a very different set of dynamics and inter-cellular behaviors may  
247 be at work in the complex *in vivo* tissue. Timing is crucial, as the VEGF gradient dissipates after  
248 the retinas are dissected and submerged in agarose, at room air and the tissue is therefore no  
249 longer hypoxic. However, the directed growth of the filopodia towards the vascular front in our

250 LSFM movies suggests that this gradient remains intact for at least the first few hours after  
251 dissection. We found filopodia length and extension, retraction dynamics quantification feasible  
252 (Fig. 7d,e,f). Further back from the sprouting front, in the vascular plexus (Fig. 4b, Movie S6),  
253 we occasionally observed the formation of connections over the course of a few hours,  
254 however, branch formation was a rare occurrence. Notably, we did not observe EC apoptosis  
255 under these imaging conditions indicating conditions are viable.

256 We next assessed the feasibility of using LSFM to live-image intracellular processes.  
257 We dynamically imaged mice expressing lifeAct-EGFP, which fluorescently labels F-actin  
258 (Fraccaroli et al. 2012) with LSFM and quantified the movements of actin-enriched bundles  
259 within the endothelial cell bodies in the sprouting front during developmental angiogenesis.  
260 Quantitative subcellular actin live-imaging was found feasible (n=6 retinas) with the average  
261 distance travelled by each bundle found to be 2.56  $\mu\text{m}$  (Fig. 4c, movies S7, S8 and S9).

262 Taken together, our LSFM permits the visualization in real-time of cellular movements  
263 with subcellular resolution in the mouse retina, with minimal distortion.

264

### 265 **Three subclasses of pathological retinal neovascular tufts revealed with LSFM**

266 We next sought to image vessels that have grown pathologically, in order to determine whether  
267 this imaging method could be used to gain greater insights into eye disease. To this end, we  
268 used the OIR model, where mouse pups are placed in 75% oxygen from P7 to P12, and are  
269 then kept at room air from P12 to P17 (Connor et al. 2009). During the hyperoxia phase, the  
270 vasculature regresses, and in the subsequent normoxia phase, new vessels grow in an  
271 abnormally enlarged and tortuous manner (Connor et al. 2009). Furthermore, vessels also start  
272 to grow into the vitreal space forming bulbous vessels, known as “vascular tufts”, above the  
273 superficial vascular layer (Fig. 5a). In the past, it has been difficult to analyze and characterize  
274 the growth of these tufts because they are large formations which appear to be distorted by the  
275 flat-mounting process. By performing IsolectinB4 and ERG immunostaining to visualize

276 endothelial cells (ECs) and their nuclei, we obtained 3D-reconstructions of the tufts and were  
277 able to first classify them into different groups by quantifying both volume and number of nuclei  
278 (Fig. 5a,e). As expected, we found that the number of nuclei increased with the size of the tuft  
279 ( $R^2 = 0.83$ ). Interestingly, however we found many small tufts, and only very few large tufts. The  
280 smallest tuft we could identify had two nuclei parallel to each other, the cells growing straight up  
281 into the vitreous (Fig. 5a, upper panel, Movie S10). We found that most tufts have between 4  
282 and 20 nuclei (“Medium tufts”, Fig. 5a, second panel row, Movie S11). We also identified a few  
283 very “large tufts” with over 20 nuclei (Fig. 5a, third panel row, Movie S12). Next, we quantified  
284 the number of connections between the vasculature and the tuft (Fig. 5b). The large tufts had a  
285 higher number of connections to the existing vasculature ( $R^2 = 0.61$ ), however surprisingly for  
286 medium and large tufts, despite very different nuclei counts, the tuft volume and number of  
287 connections to the plexus remain approximately constant (Fig. 5c). However, the number of  
288 connections and tuft volume transition sharply to ~2.5 fold and ~3 fold respectively, when the  
289 number of nuclei in the tuft exceeds twenty. This indicates that proliferation or an influx of cells  
290 to the tuft does not increase tuft volume, but rather tuft volume only significantly increases when  
291 the number of connections to the plexus also increases. Based on this observation, we propose  
292 that large tufts are in fact formed by fusion of 2 or 3 medium tufts.

293 We observed that some of the vascular tufts contained highly curved nuclei (Fig. 5a,  
294 fourth panel row, yellow arrow, Movie S13). Quantification of the number of curved nuclei/total  
295 nuclei in a tuft showed that in small and medium tufts, the number of curved nuclei correlated  
296 well with the number of total nuclei (Fig. 5d). In large tufts (over 20 total nuclei), the number of  
297 curved nuclei was stable suggesting actually a decline in curved nuclei as the number of cells in  
298 the tuft increased. Thus, the relative number of curved nuclei per tuft could also be used as a  
299 clear marker to distinguish medium and large tufts. As curved nuclei indicate cells are under  
300 severe mechanical strain, twisting or turning them around (Yuntao et al. 2018), this suggests  
301 that larger tufts may be more stable and mature, whereas the small and medium ones are under

302 more tension, still forming with significant forces curving and pulling the cells around in the tuft.  
303 Interestingly, highly curved nuclei have been shown to result in rupture of the nucleus and DNA  
304 damage (Yuntao et al. 2018), which may further exacerbate dysfunctional cell behavior in tuft  
305 formation. It should be noted that care should be taken to rotate the image stack to confirm  
306 nuclear curvature, as two nuclei parallel to each other can look like only one nucleus (Fig. 5a,  
307 fourth panel row, blue arrow), emphasizing the importance of 3D imaging with LSFM as rotating  
308 and viewing tufts from the side without distortion is not possible with confocal.

309 Finally, to quantify the level of distortion of vascular tufts incurred by flat-mounting and  
310 confocal imaging, we compared tuft depth measurements between retinas imaged with confocal  
311 and LSFM (depth defined the tuft length orientated perpendicular to plexus plane). The change  
312 in depth was particularly striking and more pronounced for larger tuft structures (Fig 5a bottom  
313 panels, e), further confirming that LSFM is superior to confocal to image larger structures in the  
314 eye.

315

### 316 **LSFM OIR Case-study: Pathological retinal neovascular tufts have a knotted morphology**

317 In order to gain better resolution to characterize the specific morphology of the different sized  
318 tufts we next performed computational image deconvolution on cropped LSFM images of  
319 vascular tufts (see Materials and Methods), which helped to decrease the scattered light caused  
320 by imaging thicker tissue with the light sheet without the need to clear the tissue (Richardson &  
321 Lichtman 2015). Upon deconvolution a dramatic and previously unappreciated “knotted”  
322 morphology of the tufts was evident across all tuft classes; often tufts had one or more holes  
323 going through (Fig. 6a,b white arrows. Also see Suppl. Fig. 2a,b for more rotational views and  
324 original rotational movies S14,S15). To describe these 3D tuft structures in detail, we next  
325 explored three systematic approaches: 1) by slowly shifting clipping planes through the tuft from  
326 the vitreous facing side to the plexus-connecting side of the tuft it was possible to better  
327 appreciate the upper and lower 3D organization of the tuft; 2) carefully rotating and hand-

328 drawing the tufts surface rendered structures from every angle and 3) comparing the colour-  
329 labeled positions of nuclei to indicate their depth position in the tuft. The first approach revealed  
330 that the tuft shown in Fig. 5a fourth panel row, had a figure of eight knot, with two clear holes  
331 through the tuft and an unexpected vessel connecting the upper vitreous surface of the tuft to  
332 the plexus (Fig. 6c and Suppl. Fig. 2b, blue stars, Movie S13). A combination of the second two  
333 approaches revealed a swirl structure to two tufts (small and medium in size) akin to a snake  
334 coiling upon itself, with several highly curved nuclei (Fig. 6d-I, Movies S16, S17) and a central  
335 hole through the entire tuft. The smaller swirled tuft had two layers, while the medium tuft had  
336 three. In both cases the top, vitreous facing surface of the tuft appeared sprout-like with  
337 protrusive shapes, a morphology consistent across many tufts, e.g. Suppl. Fig. 2c white arrow  
338 and Fig. 7a. Overall, all three approaches were extremely useful for better interpreting these  
339 complex 3D structures, providing a much deeper understanding of them than viewing as  
340 maximum 2D projections or simply rotated on a screen.

341

#### 342 **4D LSFM live-imaging of the OIR mouse model reveals altered cell dynamics**

343 To gain insights into endothelial cell behavior in vascular tufts, we next imaged the OIR-induced  
344 tufts dynamically with LSFM. Thereby, we observed that filopodia extended/retracted from  
345 abnormal vascular tufts, similar to what is seen in the extending vascular front during  
346 development of the retina vasculature. However, filopodia formed from vascular tufts remained  
347 very short (mean 4.3  $\mu\text{m}$ ) as compared to normoxia (mean 14.84  $\mu\text{m}$ ) (Fig. 7a, d). In OIR,  
348 filopodia more rapidly extended and retracted, without making connections (Fig. 7a, e, f, Movie  
349 S18). As the VEGF gradient is expected to be disrupted in the OIR model, timing from  
350 dissection to imaging is not as crucial. However, most filopodia movements occurred in the first  
351 few hours under this pathological condition. When imaging other parts of the OIR retinas to the  
352 tufts, we observed intriguing, abnormal EC behaviour. Their movements were undirected and  
353 appeared to involve blebbing-based motility (Fig. 7b, c, Movie S20). We observed both cells that

354 were dividing, and undergoing apoptosis (Fig. 7b, Movie S19), which was not observed during  
355 normal conditions. This first live imaging of altered cell behavior in the OIR mouse model further  
356 highlights the potential of LSFM for new insights into disease processes.

357

## 358 **Conclusions and Discussion**

359         Although LSFM is becoming increasingly popular, studies to date have not attempted to  
360 use it to image eye tissue. We have therefore established the first protocols to image and clear  
361 mouse eye tissue using LSFM. Because this protocol utilizes optical sectioning of whole mount  
362 tissue, we found that LSFM is a very useful tool to rapidly image and reveal eye tissue at  
363 cellular and subcellular resolution without distortion of the sample due to flat-mounting, with the  
364 benefit to view and rotate structures in full 3D. As such, the present study provides a highly  
365 relevant and improved approach to examine the inter-relationships of normal neurovascular  
366 structures and the complex morphology of aberrant vascular structures in disease models,  
367 revealing for the first time a knotted morphology to the vascular tufts in OIR. We have also  
368 established a clearing protocol for eye tissue. We have furthermore established an *ex vivo* 4D  
369 live-imaging method to follow angiogenic growth in the mouse retina in real-time, both during  
370 development and under pathological conditions, and quantified that these dynamics are  
371 significantly altered in pathological conditions. The acquisition of 3D images of vascular  
372 structures at high spatial and temporal resolution within intact ocular tissue is both novel and  
373 significant. Overall, we strongly suggest the use of LSFM for 1) the study of larger or more  
374 complex 3D tissue structures reaching across the typical retinal layers, which are liable to  
375 distortion with standard approaches and 2) dynamic cell and subcellular processes in the mouse  
376 eye. We see far-reaching potential of the approach for deeper insights into eye disease mouse  
377 models in particular. For example, it would now be feasible to skeletonize larger portions of the  
378 vascular network (ultimately, the entire retina vasculature) in order to perform flow simulations



379 and understand how the biomechanical feedback of flow impacts vessel growth in healthy and  
380 diseased eyes.

381

## 382 **LSFM vs Confocal: A Balanced Discussion**

383 **Benefits of LSFM:** In general image acquisition with LSFM is widely known to be far faster than  
384 confocal due to the illumination of the entire optical plane at once combined with the use of a  
385 camera instead of detectors, as noted earlier, an extensive stack of the entire mouse retina can  
386 be acquired very quickly using LSFM (~60 sec). 1) LSFM is better for imaging thicker or very  
387 large tissues (such as the eye cup, which is thin, but topologically spherical), due to the fast  
388 acquisition rates and the large, rotatable sample holder, removing the limited single view point  
389 from above with upright microscopes and slide mounting, 2) the illuminated plane generates  
390 less photobleaching and faster time frame rates for high temporal resolution live imaging of 3D /  
391 very thick tissues. We find LSFM imaging of the retina to be particularly informative over  
392 standard confocal microscopy when studying the following specific complex 3D and/or dynamic  
393 structures in the eye: 1) the adult retina in full - it is possible to visualize all three vascular layers  
394 in the LSFM, including direct cross-sectional viewing of the diving vessels oriented between  
395 layers by rotating the sample relative to the objective, which is not possible with confocal.  
396 Similarly, the iris and optic nerve can be observed in full, from any angle, undistorted with  
397 LSFM. 2) abnormal enlarged vessels/tufts - a newly characterized knotted morphological  
398 structure of tufts was revealed due to the improved 3D imaging and rotational viewing possible  
399 with LSFM. With confocal imaging the tuft shape can only be inferred from above and we found  
400 the depths were significantly distorted and compressed, which is likely why knots have not been  
401 described before. Interestingly the VE-cadherin staining of endothelial junctions of several OIR  
402 tufts shown in (Bentley et al 2014) indicated there were “holes” through tufts, as no junctional  
403 stains were found in clear pillars through them. However, the holes were not easy to confirm by  
404 isolectinB4 staining in the same samples, likely due to spreading of the vascular structure when

405 it was distorted during flat-mounting. We can confirm here with LSFM there are holes through  
406 tufts and that tufts appear to consist of one or more long vessel structures intertwined, swirled  
407 and potentially looped upon themselves. 3) Neurovascular interactions in one sample, as  
408 neurons and vessels are oriented perpendicular to each other through the retina, they are  
409 normally imaged with separate physical sectioning or flattening techniques in either direction,  
410 prohibiting their concurrent observation. Optical sectioning of thick tissue and then rotating the  
411 undistorted image stacks allows both to be imaged for the first time together. Indeed, obtaining  
412 such images from one sample with LSFM will permit the quantification of vessels protruding  
413 through the neuronal layers, which is now only possible by performing time-consuming serial  
414 block-face scanning electron microscopy (Denk & Horstmann 2004). 4) Live-imaging of  
415 developing mouse retinas – this has proven very difficult with *in vitro* methods providing more  
416 reliable assays, e.g. embryoid bodies (Kearney & Bautch 2003; Jakobsson et al. 2010).  
417 Although embryoid bodies contain some other cell types such as pericytes, they still do not fully  
418 reflect the complex and tissue specific *in vivo* retinal environment. Importantly, the vessel-like  
419 structure formed in the embryoid bodies have never experienced flow. Moreover, the embryoid  
420 bodies are treated with VEGF supplied to the culture medium, while *in vivo*, endothelial cells are  
421 exposed to a VEGF gradient from the astrocyte network below. Our images suggest that the  
422 VEGF gradient remains intact in the retina samples for several hours in LSFM imaging.  
423 Furthermore, our protocol enables us to follow and quantify filopodia movements from minute to  
424 minute, revealing movements never seen before. Thus, we observed astonishing abnormal  
425 cellular and subcellular level dynamics under pathological OIR conditions by 4D live LSFM  
426 imaging.

427 ***Benefits of confocal over LSFM:*** Confocal microscopy has a fundamentally higher spatial  
428 resolution with less light scatter than LSFM; clearer, more precise images of smaller structures  
429 can be obtained, such as endothelial junctions and tip cell filopodia morphology provided the

430 tissue sample is amenable to flat mounting without distortion or loss of information – i.e. it is  
431 naturally thin cross-sectionally and structures of interest have their main features in the XY  
432 plane, not in Z, XZ or YZ. Thus, confocal static imaging of normal developing vessels in a single  
433 layer of the retina will still yield better resolution images than LSFM and is very reliable for XY  
434 based quantifications such as branch point analysis. However, we find it is not reliable for  
435 acquiring accurate quantifications involving depth through Z such as vessel diameters or the  
436 morphology of cells that span between the layers (e.g. in the XZ or YZ planes). Thus, overall  
437 LSFM is not suggested to replace confocal for static developmental angiogenesis studies.  
438 However, to study and measure precise morphological attributes or dynamics of vessels with  
439 inherently 3D nature such as vessel radii, enlargements, malformations, diving vessels, iris,  
440 optic nerve or the deeper layers we find strong evidence to favour LSFM over confocal imaging.  
441 In general, the quantification time was comparable between LSFM and confocal images but  
442 there is potential for image analysis to require more effort for LSFM as files can become quickly  
443 large due to the rapid imaging (~200GB for static imaging and up to 4TB for live multichannel  
444 imaging). If an older eye is being imaged the three vascular layers will be somewhat visually  
445 overlapping (e.g. in Supp. Fig. 1b), which could be hard to manually untangle due to the  
446 curvature, and as such represents a limitation. The preservation of the tissue depth information  
447 in the large z stack however, means by computationally fitting to the local curvature of the eye  
448 tissue one could computationally colour code and subtract the retinal layers out for independent  
449 viewing and analysis, but this requires more investment than depth colour coding of flat-  
450 mounted confocal images (Milde et al. 2013).

451

## 452 **Vascular Tuft Formation**

453 The OIR model is a commonly used to study retinopathies. The three-dimensional nature of  
454 vascular tufts makes them ideal for LFSM and though this is a widely studied mouse model, the  
455 improved three-dimensional imaging allowed us to identify several new features of the important

456 pathological vessels it generates. Our observations of small, medium and large tuft classes with  
457 distinct properties and the observation of more complex knotted, swirling and looping  
458 morphologies than previously reported, suggest a new mechanistic explanation is required to  
459 understand how and why vessels twist and turn on themselves and why it appears that medium  
460 tufts reach a critical size then stop twisting and instead coalesce into larger more stable  
461 structures, akin to the development of blood islands in retinal development (Goldie et al., 2008).

462 Nuclei with unusual shapes have previously been identified in abnormally growing  
463 tissues, such as cancer (Hida et al. 2004; Kondoh et al. 2013; Versaevel et al. 2012), and to  
464 reflect mitotic instability (Gisselsson et al. 2001). It is remarkable that we observed the  
465 dramatically curved shape of EC nuclei in tufts. Although it remains unclear whether their  
466 unusual shape has consequences for EC function in the tuft, it is tempting to speculate that it  
467 would have some bearing on, or is at least be an indicator of abnormal cell behavior. Overall,  
468 the ability to rotate the tufts in 3D and view from the side, not just the top, gave a much clearer  
469 view of their structure potentiating a detailed analysis of their complex knotted structure in the  
470 future. LSFM therefore could greatly improve our understanding of these abnormal vascular  
471 formations, already opening up avenues for future studies.

472 Taken together, we propose that tuft formation proceeds as follows 1) small tufts are  
473 sprouts from the existing vasculature oriented upwards to the vitreous (e.g. as shown in Fig, 5a  
474 top panel) initiating the formation of a new tuft. However, further dynamic study is required to  
475 establish whether they are medium tufts that instead are regressing; 2) medium tufts originate  
476 from small tufts that continue to sprout, loop and potentially fuse with other upward sprouts (to  
477 generate the observed increase in connections to the plexus below), actively swirling and  
478 knotting around themselves. Further studies are needed to identify if other cell type/extracellular  
479 tissue acts as a scaffold to create the space/holes within them; 3) large tufts form when medium  
480 tufts merge with each other whereupon the knotting/swirling process declines (indicated by the  
481 plateau in curved nuclei in the large tufts and the sudden jump in tuft volume and connections to

482 the plexus) possibly indicated final stabilization or even a switch to the natural normalization of  
483 tufts in this model.

484

#### 485 **Reproducible Live imaging of angiogenesis in the retina**

486 Current retinal studies must infer dynamics from static images by hypothesizing what might  
487 have happened in real-time to generate the retina's phenotype. For example, CollagenIV-  
488 positive and IsolectinB4-negative vessels are considered to be empty membrane sleeves where  
489 the vasculature has regressed. It is therefore important to establish reproducible live-imaging  
490 methods. It will be interesting to investigate in future live-imaging studies how pervasive the kiss  
491 and run behaviors are across the plexus and under different conditions, in order to fully  
492 elucidate their functional role. We furthermore demonstrated the potential to quantify diverse  
493 subcellular level movements in the cells as proof of concept. The LSM live imaging protocol is  
494 sturdy as indicated from the testing in three different laboratories in three different countries  
495 (US, Sweden and Portugal) with different scientists performing the dissections and imaging, on  
496 different instruments. As such we can confirm that though challenging, the live imaging protocol  
497 has been optimized and is reproducible in different hands.

498

#### 499 **Materials and Methods**

##### 500 **Mice**

501 mT/mG mice were crossed with cdh5 (PAC) CreERT2 mice (Wang et al. 2010). For live-imaging  
502 of retinal angiogenesis during development, mice were injected with 50 µg tamoxifen at  
503 postnatal day (P) 1, P2 and P3, and imaged at P4 (Wang et al. 2010). For live-imaging of  
504 oxygen-induced retinopathy (OIR) experiments, mice were injected with 100 µg tamoxifen at  
505 P13, P14 and P15. The retinal vasculature was imaged at P17. Recombination was confirmed  
506 by GFP expression in ECs. Mice used in experiments at Beth Israel Deaconess Medical Center  
507 were held in accordance with Beth Israel Deaconess Medical Center IACUC guidelines. Animal

508 work performed at Uppsala University was approved by the Uppsala University board of animal  
509 experimentation. Transgenic mice were maintained at the Instituto de Medicina Molecular (iMM)  
510 under standard husbandry conditions and under national regulations.

511

## 512 **Antibodies**

513 IsolectinB4 directly conjugated to Alexa488 and all corresponding secondary alexa conjugated  
514 antibodies were obtained from Invitrogen. Isolectin IB4 conjugated with an Alexa Fluor 568 dye  
515 was purchased from Thermo Fisher Scientific, MA. Anti-calretinin (ab702) and anti-ERG  
516 (ab2513) antibodies were obtained from Abcam. The antibody directed against Calbindin  
517 (AB1778) was acquired from Millipore. Anti-Glial Fibrillary Acidic Protein (GFAP) antibody was  
518 purchased from Dako (Z0334), anti-CollagenIV from AbD Serotec (2150-1470), biotinylated anti-  
519 neuron-specific b-III Tubulin from R&D Systems (Clone TuJ-1, BAM1195), and Cy3-conjugated  
520 anti-smooth muscle actin (SMA) antibody was obtained from Sigma Life Science (C6198).  
521 Draq5 was obtained from ThermoScientific. Anti-GOLPH4 (ab28049) from Abcam.

522

## 523 **Immunohistochemistry**

524 Retinas were dissected as previously described (Del Toro et al. 2010). In brief, eyeballs were  
525 fixed for 18 min in 4% paraformaldehyde at room temperature. After dissection, retinas were  
526 blocked for 1 hour in blocking buffer (TNBT) or Claudio's Blocking Buffer (CBB) for retinas with  
527 Golgi stained. CBB consists of 1% FBS (ThermoFisher Scientific), 3% BSA (Nzytech), 0.5%  
528 Triton X100 (Sigma), 0.01% Sodium deoxycholate (Sigma), 0,02% Sodium Azide (Sigma) in  
529 PBS pH = 7.4 for 2 hr in a rocking platform) for retinas stained for golgi. Thereafter, retinas were  
530 incubated overnight in primary antibody in blocking buffer. After extensive washing, retinas were  
531 incubated in the corresponding secondary antibody for 2 hours at room temperature. For  
532 confocal microscopy, retinas were mounted on glass slides, and for LSFM, retinas were  
533 mounted in 2% low-melting agarose. Agarose was melted at >65°C, and then maintained at

534 42°C before adding the tissue. To minimize curling of the retina, apply 1-2 drops of low melting  
535 agarose on retina and start uncurling the retina before the gel is solidified. It can then be  
536 transferred to the cylinder for imaging.

537

### 538 **PACT clearing of retinas**

539 PACT clearing was performed as previously described (Treweek et al. 2015b). Retinas were  
540 dissected and fixed with 4% PFA at 4°C overnight. Samples were incubated overnight at 4°C in  
541 ice cold A4P0 (40% acrylamide, Photoinitiator in PBS). The following day, samples were  
542 degassed on ice by applying a vacuum to the tube for 30 min, followed by purging with N<sub>2</sub> for 30  
543 min. Thereafter, samples were incubated at 37°C for 3h to allow hydrogel polymerization.  
544 Excess gel was then removed from the samples, the samples washed in PBS, and incubated at  
545 37°C for 6h in 8% SDS/PBS, pH 7.5. Samples were then washed in PBST for 1-2 days,  
546 changing wash buffer 4-5 times to remove all of the SDS. Immunostaining was then performed  
547 following the same protocol without PACT clearing. Thereafter, the tissue was cleared by at  
548 least 48h incubation in RIMS (40 g histodenz in 30 ml of sterile-filtered 0.02 M phosphate buffer,  
549 0.01% sodium azide). Cleared retinas were mounted in 5% low-melting agarose/RIMS for LSFM  
550 imaging.

551

### 552 **Live-imaging**

553 For live-imaging, mice were imaged at P4 or P5. The sample chamber was filled with DMEM  
554 without phenol red containing 50% FBS and P/S and heated to 37°C. Retinas were quickly  
555 dissected in prewarmed HBSS containing penicillin and streptomycin. After dissection, retinas  
556 were rapidly cut into quarters (mainly to minimize the datafile size created, the curved form was  
557 preserved) and immediately mounted in 1% low melting agarose in DMEM without phenol red  
558 containing 50% Fetal Bovine Serum (FBS) and 1x penicillin and streptomycin (P/S). To

559 minimize curling of the retina, as with static imaging, apply 1-2 drops of low melting agarose on  
560 retina and start uncurling the retina before the gel is solidified. It can then be transferred to the  
561 cylinder for imaging.

562

### 563 **Equipment**

564 All LSFM images were acquired with a Zeiss Z.1 light sheet microscope. The Zeiss objectives  
565 used for uncleared tissue and live imaging were Zeiss, RI=1.33, 5x/0.16, and 20x/1.0. For PACT  
566 cleared tissue, RI=1.45, 20x/1.0 (5.5mm working distance) was used. All raw data were handled  
567 on a high-end DELL workstation (Dual 8-core Xeon Processors, 196GB RAM, NVIDIA Titan  
568 Black GPU, Windows 7 64 bit) running ZEISS ZEN (Light sheet edition). Confocal images were  
569 taken with the LSM 880 Confocal Microscope.

570

### 571 **Image Analysis**

#### 572 **Visualization of images in 3D**

573 3D reconstructions of images up to 4 GB were obtained using Imaris software. Fiji was used for  
574 reconstruction of images larger than 4 GB. To quantify tuft volumes, Arivis Vision4D software  
575 was used.

576

#### 577 **Visualization of live-imaging**

578 To visualize live-images, the maximum intensity projection of each timepoint was made in ZEN  
579 (Zeiss). The movies were corrected for drift correction in Fiji using the StackReg plugin and the  
580 background subtracted in Fiji using rolling ball background subtraction.

581

### 582 **Deconvolution**



583 In LSFM, when using a high NA ( $> \sim 0.6$ ) objective, the optical section is determined by the depth  
584 of field of the objective and not the light sheet. However, in our system the light sheet is thicker  
585 than the objective's depth of field and substantial out-of-focus light is captured relative to  
586 confocal. Additionally, thick tissue samples have an intrinsic milky appearance. This lack of  
587 clarity undermines sharp images and becomes progressively more of an impediment the deeper  
588 one tries to look into a tissue volume. This translucency is caused by heterogeneous light  
589 scattering (Richardson & Lichtman 2015). As the tissue used for imaging in LSFM is thick,  
590 fluorescent light originating from deep within the tissue is scattered during its travel through the  
591 tissue volume, back to the objective. This results in both in- and out-of-focus light arriving at an  
592 incorrect position on the camera causing objects to blur.

593 To deconvolve and reduce this light scatter computationally images were split into channels with  
594 their respective emission wavelength. Microscopic parameters (including pixel size, objective  
595 and excitation wavelength) were inserted into the settings of Huygens software for each channel  
596 followed by choosing the signal to noise ratio (SNR) for each image and run the deconvolution  
597 with the same settings. The resulted deconvolved images were inserted into Imaris for further  
598 analysis in 3D if needed. Huygens software was used for deconvolving all images.

599 **Actin-rich bundles and filopodia tracking.** Tracking was performed manually using  
600 ImageJ/Fiji. For filopodia tracking, each filopodia was tracked between each frame of imaging  
601 and different analysis was performed. For tracking the actin-rich bundles, the Manual Tracking  
602 plugin in Fiji was used to manually select the ROI (=region of interest) and follow the pathway of  
603 each trajectory. The trajectories and the pathway were overlaid. Each trajectory could be  
604 visualized using Montage function.

605

606 **Acknowledgements**

607 We would like to thank Sven Terclavers (HCBI) for the excellent technical support and Joe  
608 Brock and the Illustration team at The Francis Crick Institute for aiding with 3D drawing of tuft  
609 knots. C.P and K.B. were supported by funding from Harvard Catalyst | The Harvard Clinical  
610 and Translational Science Center (National Center for Research Resources and the National  
611 Center for Advancing Translational Sciences, National Institutes of Health Award UL1  
612 TR001102), the NEI (1R21EY027067-01), and BIDMC. K. B and P.A were supported by The  
613 Kjell and Märta Beijer Foundation. K.B. and L.C.W. were supported by a grant from the Knut  
614 and Alice Wallenberg foundation (KAW 2015.0030). L.V. was supported by a Victor A. McKusick  
615 fellowship from the Marfan Society. M.R. was supported by an EMBO fellowship (ALTF 2016-  
616 923). K.I.H. was supported by institutional training grant T32 HL07893 from the NHLBI of the  
617 NIH. L.V. was funded by the Victor A. McKusick Fellowship from the Marfan Foundation and  
618 BIDMC. D.F.C supported by EY025259, Lions Foundation, and NEI core grant P30 EY03790.  
619 K-S Cho: EY027067. C.A.F was supported by European Research Council starting grant  
620 (679368), the Fundação para a Ciência e a Tecnologia funding (grants: IF/00412/2012;  
621 PRECISE-LISBOA-01-0145-FEDER-016394; and a grant from the Fondation Leducq  
622 (17CVD03).

### 623 **Competing Interests**

624 The authors declare no competing interests.

625  
626

627

### 628 **References**

- 629 Abe, J. et al., 2016. Light sheet fluorescence microscopy for in situ cell interaction analysis in  
630 mouse lymph nodes. *Journal of Immunological Methods*, pp.1–10. Available at:  
631 <http://linkinghub.elsevier.com/retrieve/pii/S0022175916300151>.
- 632 Akula, J.D. et al., 2007. Rod Photoreceptor Function Predicts Blood Vessel Abnormality in  
633 Retinopathy of Prematurity. *Investigative Ophthalmology & Visual Science*, 48(9), p.4351.  
634 Available at: <http://iovs.arvojournals.org/article.aspx?doi=10.1167/iovs.07-0204>.
- 635 Baeyens, N. et al., 2016. Endothelial fluid shear stress sensing in vascular health and disease.  
636 *Journal of Clinical Investigation*, 126(3), pp.821–828. Available at:  
637 <https://www.jci.org/articles/view/83083>.

- 638 Bentley, K., Franco, C.A., Philippides, A., Blanco, R., Dierkes, M., Gebala, V., Stanchi, F.,  
639 Jones, M., Aspalter, I.M., et al., 2014. The role of differential VE-cadherin dynamics in cell  
640 rearrangement during angiogenesis. *Nature Cell Biology*, 16(4), pp.309–321. Available at:  
641 <http://www.nature.com/doi/10.1038/ncb2926>.
- 642 Bernabeu, M., Jones, M.L., Nielsen, J.H., Krüger, T., Nash, R.W., Groen, D., Schmieschek, S.,  
643 Hetherington, J., Gerhardt, H., Franco, C. A., Coveney, P. Computer simulations reveal  
644 complex distribution of haemodynamic forces in a mouse retina model of angiogenesis  
645 R. Soc. Interface <http://doi.org/10.1098/rsif.2014.0543>
- 646 Borgefors, G., 1984. Distance transformations in arbitrary dimensions. *Computer Vision,*  
647 *Graphics, and Image Processing*, 27, pp.321–345. Available at:  
648 <http://www.sciencedirect.com/science/article/pii/0734189X84900355>.
- 649 Brown, E. et al., 2010. In vivo imaging of tumors. *Cold Spring Harbor Protocols*, 5(7), pp.1–5.
- 650 Connor, K.M. et al., 2009. Quantification of oxygen-induced retinopathy in the mouse: a model  
651 of vessel loss, vessel regrowth and pathological angiogenesis. *Nature protocols*, 4(11),  
652 pp.1565–1573.
- 653 Danielsson, P.-E., 1980. Euclidean distance mapping. *Computer Graphics and Image*  
654 *Processing*, 14(3), pp.227–248. Available at:  
655 <http://linkinghub.elsevier.com/retrieve/pii/0146664X80900544>.
- 656 Denk, W. & Horstmann, H., 2004. Serial Block-Face Scanning Electron Microscopy to  
657 Reconstruct Three-Dimensional Tissue Nanostructure Kristen M. Harris, ed. *PLoS Biology*,  
658 2(11), p.e329. Available at: <http://dx.plos.org/10.1371/journal.pbio.0020329>.
- 659 Ellenbroek, S.I.J. & van Rheenen, J., 2014. Imaging hallmarks of cancer in living mice. *Nature*  
660 *Reviews Cancer*, 14(6), pp.406–418. Available at:  
661 <http://www.nature.com/doi/10.1038/nrc3742>.
- 662 Fei, P. et al., 2016. Cardiac Light-Sheet Fluorescent Microscopy for Multi-Scale and Rapid  
663 Imaging of Architecture and Function. *Nature Publishing Group*, (October 2015), pp.1–12.  
664 Available at: <http://dx.doi.org/10.1038/srep22489>.
- 665 Franco, C.A., Jones, M.L., Bernabeu, M.O., Geudens, I., Mathivet, T., Rosa, A., Lopes, F.M.,  
666 Lima, A.P., Ragab, A., Collins, R.T., Phng, L-K., Coveney, P., Gerhardt, H., 2015. Dynamic  
667 endothelial cell rearrangements drive developmental vessel regression. *PLoS biology* 13 (4),  
668 e1002125
- 669 Gerhardt, H. et al., 2003. VEGF guides angiogenic sprouting utilizing endothelial tip cell  
670 filopodia. *Journal of Cell Biology*, 161, pp.1163–1177.
- 671 Gisselsson, D. et al., 2001. Abnormal Nuclear Shape in Solid Tumors Reflects Mitotic Instability.  
672 *The American Journal of Pathology*, 158(1), pp.199–206.
- 673 Goldie, L.C., Nix, M.K. & Hirschi, K.K., 2008. Embryonic vasculogenesis and hematopoietic  
674 specification. *Organogenesis*, 4(4), pp.257–63. Available at:  
675 <http://www.ncbi.nlm.nih.gov/pubmed/19337406>.
- 676 Güç, E. et al., 2014. Long-term Intravital Immunofluorescence Imaging of Tissue Matrix  
677 Components with Epifluorescence and Two-photon Microscopy. *Journal of Visualized*  
678 *Experiments*, (86), pp.e51388–e51388. Available at:  
679 [http://www.jove.com/video/51388/long-term-intravital-immunofluorescence-imaging-tissue-](http://www.jove.com/video/51388/long-term-intravital-immunofluorescence-imaging-tissue-matrix)  
680 [matrix](http://www.jove.com/video/51388/long-term-intravital-immunofluorescence-imaging-tissue-matrix).
- 681 Hägerling, R. et al., 2013. A novel multistep mechanism for initial lymphangiogenesis in mouse

- 682 embryos based on ultramicroscopy. *The EMBO journal*, 32(January), pp.629–44. Available  
683 at:  
684 [http://www.pubmedcentral.nih.gov/articlerender.fcgi?artid=3590982&tool=pmcentrez&rend](http://www.pubmedcentral.nih.gov/articlerender.fcgi?artid=3590982&tool=pmcentrez&rendertype=abstract)  
685 [ertype=abstract](http://www.pubmedcentral.nih.gov/articlerender.fcgi?artid=3590982&tool=pmcentrez&rendertype=abstract).
- 686 Hama, H. et al., 2011. Scale: a chemical approach for fluorescence imaging and reconstruction  
687 of transparent mouse brain. *Nature Neuroscience*, 14(11), pp.1481–1488. Available at:  
688 <http://dx.doi.org/10.1038/nn.2928>.
- 689 Hartnett, M.E., 2015. Pathophysiology and Mechanisms of Severe Retinopathy of Prematurity.  
690 *Ophthalmology*, 122(1), pp.200–210. Available at:  
691 <http://linkinghub.elsevier.com/retrieve/pii/S0161642014006940>.
- 692 Hida, K. et al., 2004. Tumor-associated endothelial cells with cytogenetic abnormalities. *Cancer*  
693 *research*, 64(22), pp.8249–55. Available at:  
694 <http://www.ncbi.nlm.nih.gov/pubmed/15548691>.
- 695 Hou, B. et al., 2015. Scalable and Dil-compatible optical clearance of the mammalian brain.  
696 *Frontiers in Neuroanatomy*, 9(February), p.19. Available at:  
697 [http://www.pubmedcentral.nih.gov/articlerender.fcgi?artid=4338786&tool=pmcentrez&rend](http://www.pubmedcentral.nih.gov/articlerender.fcgi?artid=4338786&tool=pmcentrez&rendertype=abstract)  
698 [ertype=abstract](http://www.pubmedcentral.nih.gov/articlerender.fcgi?artid=4338786&tool=pmcentrez&rendertype=abstract).
- 699 Huber, G. et al., 2009. Spectral domain optical coherence tomography in mouse models of  
700 retinal degeneration. *Investigative ophthalmology & visual science*, 50, pp.5888–5895.
- 701 Jakobsson, L. et al., 2010. Endothelial cells dynamically compete for the tip cell position during  
702 angiogenic sprouting. *Nature Cell Biology*, 12(10), pp.943–953. Available at:  
703 <http://www.nature.com/doi/10.1038/ncb2103>.
- 704 Kearney, J.B. & Bautch, V.L., 2003. In Vitro Differentiation of Mouse ES Cells: Hematopoietic  
705 and Vascular Development. *Methods in Enzymology*, 365, pp.83–98.
- 706 Kondoh, M. et al., 2013. Hypoxia-Induced Reactive Oxygen Species Cause Chromosomal  
707 Abnormalities in Endothelial Cells in the Tumor Microenvironment R. Morishita, ed. *PLoS*  
708 *ONE*, 8(11), p.e80349. Available at: <http://dx.plos.org/10.1371/journal.pone.0080349>.
- 709 Kubota, Shimpei I., Kei Takahashi, Jun Nishida, Yasuyuki Morishita, Shogo Ehata, Kazuki  
710 Tainaka, Kohei Miyazono, and Hiroki R. Ueda., 2017. Whole-body profiling of cancer metastasis  
711 with single-cell resolution. *Cell reports* 20, no. 1: 236-250.  
712
- 713 Lawson, N.D. & Weinstein, B.M., 2002. In Vivo Imaging of Embryonic Vascular Development  
714 Using Transgenic Zebrafish. *Developmental Biology*, 248(2), pp.307–318.
- 715 Liebmann, T., Renier, N., Bettayeb, K., Greengard, P., Tessier-Lavigne, M. & Flajolet, M., 2016.  
716 Three-Dimensional Study of Alzheimer’s Disease Hallmarks Using the iDISCO Clearing  
717 Method. *Cell Reports*, 16(4), pp.1138–1152.
- 718 Liebmann, T., Renier, N., Bettayeb, K., Greengard, P., Tessier-Lavigne, M. & Correspondence,  
719 M.F., 2016. Three-Dimensional Study of Alzheimer’s Disease Hallmarks Using the iDISCO  
720 Clearing Method.
- 721 Milde, F., Lauw, S., Koumoutsakos, P. and Iruela-Arispe, M.L., 2013. The mouse retina in 3D:  
722 quantification of vascular growth and remodeling. *Integrative Biology*, 5(12), pp.1426-1438.
- 723 Motoike, T. et al., 2000. Universal GFP for the study of vascular development. *Genesis*, 28,  
724 pp.75–81.

- 725 Murray, E., Cho, J.H., Goodwin, D., Ku, T., Swaney, J., Kim, S.Y., Choi, H., Yoon Park, J.,  
726 Hubbert, A., McCue, M., Gyun Park, Y., Vassallo, S., Bakh, N., Frosch, M., Wedeen, V J.,  
727 Seung, H.S., Chung, K., 2015. Simple, scalable proteomic imaging for high dimensional profiling  
728 of intact systems. *Cell* 63(6):1500-14. doi: 10.1016/j.cell.2015.11.025. PubMed PMID: 26638076
- 729 Muzumdar, M.D. et al., 2007. A global double-fluorescent Cre reporter mouse. *genesis*, 45(9),  
730 pp.593–605. Available at: <http://doi.wiley.com/10.1002/dvg.20335>.
- 731 Narayanan, S.P. et al., 2014. Arginase 2 deficiency reduces hyperoxia-mediated retinal  
732 neurodegeneration through the regulation of polyamine metabolism. *Cell Death and*  
733 *Disease*, 5, p.e1075. Available at: <http://www.nature.com/doi/10.1038/cddis.2014.23>.
- 734 Nentwich, M.M. & Ulbig, M.W., 2015. Diabetic retinopathy - ocular complications of diabetes  
735 mellitus. *World journal of diabetes*, 6(3), pp.489–99. Available at:  
736 [http://www.pubmedcentral.nih.gov/articlerender.fcgi?artid=4398904&tool=pmcentrez&rend](http://www.pubmedcentral.nih.gov/articlerender.fcgi?artid=4398904&tool=pmcentrez&rendertype=abstract)  
737 [ertype=abstract](http://www.pubmedcentral.nih.gov/articlerender.fcgi?artid=4398904&tool=pmcentrez&rendertype=abstract).
- 738 Nicoli, S. et al., 2010. MicroRNA-mediated integration of haemodynamics and Vegf signalling  
739 during angiogenesis. *Nature*, 464(7292), pp.1196–1200. Available at:  
740 <http://www.nature.com/doi/10.1038/nature08889>.
- 741 Pietzsch, T. et al., 2015. BigDataViewer: visualization and processing for large image data sets.  
742 *Nature Methods*, 12(2012), pp.481–483. Available at:  
743 <http://www.nature.com/doi/10.1038/nmeth.3392>.
- 744 Preibisch, S. et al., 2014. Efficient Bayesian-based multiview deconvolution. *Nature methods*,  
745 11(6), pp.645–8. Available at: <http://dx.doi.org/10.1038/nmeth.2929>.
- 746 Renier, N. et al., 2014. iDISCO: A Simple, Rapid Method to Immunolabel Large Tissue Samples  
747 for Volume Imaging - suppl original. *Cell*, 159. Available at:  
748 <http://www.sciencedirect.com/science/article/pii/S0092867414012975>.
- 749 Renier, N. et al., 2016. Mapping of Brain Activity by Automated Volume Analysis of Immediate  
750 Early Genes. *Cell*, 165(7), pp.1789–1802.
- 751 Reynaud, E.G. et al., 2014. Guide to light-sheet microscopy for adventurous biologists. *Nature*  
752 *Methods*, 12(1), pp.30–34. Available at: <http://dx.doi.org/10.1038/nmeth.3222>.
- 753 Rezzola, S. et al., 2013. A novel ex vivo murine retina angiogenesis (EMRA) assay.  
754 *Experimental Eye Research*, 112, pp.51–56.
- 755 Richardson, D.S. & Lichtman, J.W., 2015. Clarifying Tissue Clearing. *Cell*, 162(2), pp.246–257.  
756 Available at: <http://linkinghub.elsevier.com/retrieve/pii/S0092867415008375>.
- 757 Sawamiphak, S., Ritter, M. & Acker-Palmer, A., 2010. Preparation of retinal explant cultures to  
758 study ex vivo tip endothelial cell responses. *Nature protocols*, 5(10), pp.1659–1665.  
759 Available at: <http://dx.doi.org/10.1038/nprot.2010.130>.
- 760 Schindelin, J. et al., 2012. Fiji: an open-source platform for biological-image analysis. *Nature*  
761 *methods*, 9(7), pp.676–82. Available at: [http://www.nature.com.ezp-](http://www.nature.com.ezp-prod1.hul.harvard.edu/nmeth/journal/v9/n7/full/nmeth.2019.html)  
762 [prod1.hul.harvard.edu/nmeth/journal/v9/n7/full/nmeth.2019.html](http://www.nature.com.ezp-prod1.hul.harvard.edu/nmeth/journal/v9/n7/full/nmeth.2019.html).
- 763 Schmid, B. et al., 2010. A high-level 3D visualization API for Java and ImageJ. *BMC*  
764 *Bioinformatics*, 11(1), p.274. Available at:  
765 <http://bmcbioinformatics.biomedcentral.com/articles/10.1186/1471-2105-11-274>.
- 766 Schoors, S. et al., 2014. Incomplete and transitory decrease of glycolysis A new paradigm for  
767 anti-angiogenic therapy? *Cell Cycle*, 131, pp.16–22.
- 768 Sommer, C. et al., 2011. Ilastik: Interactive learning and segmentation toolkit. In *2011 IEEE*



- 769 *International Symposium on Biomedical Imaging: From Nano to Macro*. IEEE, pp. 230–233.  
770 Available at: <http://ieeexplore.ieee.org/lpdocs/epic03/wrapper.htm?arnumber=5872394>.
- 771 Srinivasan, V.J. et al., 2006. Noninvasive volumetric imaging and morphometry of the rodent  
772 retina with high-speed, ultrahigh-resolution optical coherence tomography. *Investigative*  
773 *Ophthalmology and Visual Science*, 47, pp.5522–5528.
- 774 Stahl, A. et al 2010; The Mouse Retina as an Angiogenesis Model. *Invest. Ophthalmol. Vis. Sci.*  
775 2010;51(6):2813-2826. doi: 10.1167/iovs.10-5176.
- 776 Stelzer, E.H.K., 2014. Light-sheet fluorescence microscopy for quantitative biology. *Nature*  
777 *Methods*, 12(1), pp.23–26. Available at: <http://dx.doi.org/10.1038/nmeth.3219>.
- 778 Del Toro, R. et al., 2010. Identification and functional analysis of endothelial tip cell-enriched  
779 genes. *Blood*, 116(19), pp.4025–4033.
- 780 Treweek, J.B. et al., 2015a. Whole-body tissue stabilization and selective extractions via tissue-  
781 hydrogel hybrids for high-resolution intact circuit mapping and phenotyping. *Nature*  
782 *Protocols*, 10, pp.1860–1896. Available at: <http://dx.doi.org/10.1038/nprot.2015.122>.
- 783 Treweek, J.B. et al., 2015b. Whole-body tissue stabilization and selective extractions via tissue-  
784 hydrogel hybrids for high-resolution intact circuit mapping and phenotyping. *Nature*  
785 *Protocols*, 10, pp.1860–1896.
- 786 Ubezio, B. et al., 2016. Synchronization of endothelial Dll4-Notch dynamics switch blood  
787 vessels from branching to expansion. *eLife*, 5, pp.186–193. Available at:  
788 <http://www.ncbi.nlm.nih.gov/pubmed/27074663>.
- 789 Udan, R.S. et al., 2014. Quantitative imaging of cell dynamics in mouse embryos using light-  
790 sheet microscopy. *Development*, 141(October), pp.4406–4414. Available at:  
791 <http://dev.biologists.org/cgi/doi/10.1242/dev.111021>.
- 792 Usui, Y. et al., 2015. Neurovascular crosstalk between interneurons and capillaries is required  
793 for vision. *The Journal of clinical investigation*, 125(6), pp.2335–46. Available at:  
794 <http://www.ncbi.nlm.nih.gov/pubmed/25915585>.
- 795 Verheyen, A. et al., 2012. Systemic anti-vascular endothelial growth factor therapies induce a  
796 painful sensory neuropathy. *Brain*, 135, pp.2629–2641.
- 797 Versaevel, M., Grevesse, T. & Gabriele, S., 2012. Spatial coordination between cell and nuclear  
798 shape within micropatterned endothelial cells. *Nature Communications*, 3, p.671. Available  
799 at: <http://www.nature.com/doi/10.1038/ncomms1668>.
- 800 Wang, Y. et al., 2010. Ephrin-B2 controls VEGF-induced angiogenesis and lymphangiogenesis.  
801 , 465(May).
- 802 Yang, B. et al., 2014. Single-Cell Phenotyping within Transparent Intact Tissue through Whole-  
803 Body Clearing. *Cell*, pp.1–14. Available at: <http://dx.doi.org/10.1016/j.cell.2014.07.017>.
- 804 Yuntao, X., Ivanovska, I.L., Zhu, K., Smith, L., Irianto, J., Pfeifer, C.R., Alvey, C. 2018. Nuclear  
805 rupture at sites of high curvature compromises retention of DNA repair factors. *J Cell Biol* 217,  
806 no. 11: 3796-3808.

807

808

## 809 **Figure Legends**

810 **Figure 1: Imaging of the whole eye using light sheet microscopy.** **a**, Schematic of retina  
811 preparation for imaging. For conventional confocal microscopy, four incisions are made to  
812 enable flat-mounting of the retina onto a cover slip. For LSFM, pieces of the retina are  
813 suspended and imaged from a right angle. **b**, Maximum intensity projection (MIP) of a P15  
814 mouse eyeball ( $z = 274$  slices). Vessels were visualized with IsoB4 staining. Scale bar, 500  $\mu\text{m}$ .  
815 **c**, 3D-rendered image of the adult iris microvasculature ( $z = 263$  slices). Vessels were  
816 visualized with IsoB4 (yellow arrows). Scale bar, 250  $\mu\text{m}$ . **d**, MIP of the optic nerve. Vessels  
817 were visualized with IsoB4 staining ( $z = 176$  slices). Scale bar, 50  $\mu\text{m}$ . **e**, MIP of a cross section  
818 of a P10 mouse retina. Vessels were visualized with IsoB4 staining. Scale bar, 100  $\mu\text{m}$ . **f**, MIP  
819 of a whole P10 mouse retina suspended and imaged intact ( $z = 176$  slices). Vessels were  
820 visualized with IsoB4 staining. Scale bar, 500  $\mu\text{m}$ . See supplementary figure 1 for additional  
821 images.

822 **Figure 2: 3D reconstruction of nerves and vessels in one image.** **a**, Schematic of an  
823 eyeball. **b**, Schematic of the retina and its cell types. **c**, Retinal eye cups expressing yellow  
824 fluorescent protein, YFP (green) were harvest from Thy1-YFP mice and stained with Isolectin  
825 IB4 (red). The retinal eye cups were mounted and imaged with LSFM. **d**, enlarged region of **c**. **e**,  
826 Representative image of an eyeball before clearing (left panel), and an eyeball after PACT  
827 clearing (right panel). The circle around the cleared eyeball depicts the outline of the eyeball.  
828 Scale bar, 2 mm. **f**, Draq5 staining (magenta) visualizes the inner nuclear layer (INL) and outer  
829 nuclear layer (ONL) of the adult mouse PACT cleared retina. Vessels were visualized by IsoB4  
830 staining (green). **g**, Tuj1 (green) and calbindin (red) visualize the ganglion and horizontal cells in  
831 the mouse PACT cleared retina. **h**, Smooth muscle actin (SMA, red) and Collagen IV staining  
832 (Coll.IV, green) visualize the three vascular layers and smooth muscle cells in the mouse PACT  
833 cleared retina. Scale bars, 50  $\mu\text{m}$ .

834 **Figure 3. Vessel depth distortion in confocal due to flatmounting.** **a**, Schematic showing  
835 the correlative LSFM-Confocal imaging approach used to quantify vessel distortion incurred by  
836 flatmounting. **b**, the same large vessel segment imaged first with LSFM then confocal (surface  
837 rendered in Imaris). By orienting with the surrounding vessel connections to determine the  
838 plexus plane (equivalent to the XY plane in confocal) and the plane perpendicular to it (“perp  
839 plane”), which is equivalent to the Z plane in confocal, comparative width (W) and depth (D)  
840 measurements can be made of the same vessel segment. **c**, cross sectional views of another  
841 representative large vessel near the optic nerve shows how the aspect ratio of W and D is  
842 shifted to an ellipse in confocal. Near Optic: n = 60 vessels from 6 retinas (7 images). Vascular  
843 Front n = 28 vessels in from 4 retinas (4 images) for each confocal and lsfm.

844 **Figure 4: Live-imaging of the retinal vasculature.** **a**, Single maximum intensity projections  
845 (MIP) of an hour time lapse movie show long, slender filopodia, and rapid fusion and  
846 disconnection of tip cells at the vascular front of mT/mG x cdh5 (PAC) CreERT2 mice (stars). **b**,  
847 MIPs of a time lapse movie reveal the connection between two branches in the capillary plexus  
848 (star).

849 **Figure 5: Analysis of three subclasses of OIR vascular tuft.** **a**, Representative 3D-rendered  
850 LSFM images of small (1<sup>st</sup> row), medium (2<sup>nd</sup> row), and large (3<sup>rd</sup> row) tufts showing the  
851 vasculature (IsoB4, green) and endothelial nuclei (ERG, magenta), scale bar = 10  $\mu$ m. For all  
852 widefield images, scale bar = 40  $\mu$ m, yellow box indicates tuft in situ; 4<sup>th</sup> row - representative  
853 3D-rendered images showing curved nuclei in a medium tuft, yellow arrows indicate curved  
854 nuclei, blue arrows indicate flat nuclei parallel to each other. Scale bar, 10  $\mu$ m. 5<sup>th</sup> row:  
855 correlative LSFM-confocal microscopy of the same tuft reveals the tuft depth distortion (side  
856 view) incurred with confocal flatmounting versus LSFM. **b**, The volume of the tufts versus the  
857 number of nuclei per tuft. **c**, The number of vessel connections between the tuft and the  
858 underlying vascular plexus versus the number of nuclei. **d**, Quantification of the number of



859 curved nuclei per tuft versus the total number of total nuclei per tuft. **e**, quantifications of tuft  
860 depths per subclass size in LSFM vs confocal images, significant difference shown using  
861 unpaired t test, \*\*\* means  $P < 0.0001$ .

862 **Figure 6. Knotted morphology of neovascular tufts revealed with LSFM.** **a,d,g**,  
863 representative 3D-rendered images (generated using IMARIS software) of large (upper panel),  
864 medium and small tufts showing the vasculature (IsoB4, green) and endothelial nuclei (ERG,  
865 red) from rotational movies S14,15 See Supp. Fig. 2a for further views from different angles of  
866 the large tufts. White dashed arrows indicates a hole through the tuft. Scale bar, 30  $\mu\text{m}$ . **b**,  
867 widefield LSFM of OIR retina demonstrates that the knotted morphology is hard to discern from  
868 afar. **c**, detailed 3D clipping plane and 3D rotational drawings of an individual knot reveal a  
869 figure of eight structure with two clear holes through the tuft as well a vessel connecting from the  
870 upper, vitreous facing surface of the tuft to the plexus below (blue star). Stars mark  
871 corresponding regions from the illustration to the images - lower tuft loop nearer plexus (yellow  
872 star), upper tuft loop nearer vitreous (red star). See also Suppl. Fig. 2b for detailed 3D drawings  
873 made from each rotational view of this tuft with clipping planes, and Movie S13. **e,h**, 3D  
874 sketches made from rotational movies S16,17 to better elucidate nuclei: blue nuclei - bottom of  
875 tuft (near plexus), red nuclei – middle of tuft (in **e**), top of tuft (facing vitreous) in **h**, yellow nuclei  
876 - top of tuft (facing vitreous) in **e,f,i**, schematic illustrating the swirling tuft morphology observed  
877 in **d-h** with three layers for the medium tuft (**f**) and two for the small one (**i**).

878 **Figure 7.** OIR live imaging **a**, Maximum intensity projections (MIPs) of a time lapse movie of a  
879 retinal tuft of a mouse in the oxygen-induced retinopathy (OIR) model visualize short, rapidly  
880 extending and retracting filopodia as compared to control retinas (stars). **b**, MIPs of a time lapse  
881 movie of mouse retinal vasculature in the OIR model reveal cell shuffling in real-time (arrow). **c**,  
882 MIPs of a time lapse movie of mouse retinal vasculature in the OIR model reveal abnormal  
883 vessel growth in real-time. Scale bar, 20  $\mu\text{m}$ . **d**, the maximum length that each filopodia reached

884 was measured for each filopodia over time in P5 and OIR conditions. **e**, the total time that each  
885 filopodia was present during the experiment; this time is calculated from when one filopodia  
886 appeared and then disappeared. **f**, speed of extension and retraction of filopodia were  
887 calculated for P5 and OIR conditions. Total n= 67 and 23 filopodia in 8 and 3 cropped movies  
888 from 3 independent P5 and 1 OIR experiment.

## 889 **Supplemental Figure Legends**

890

891 **Supplemental Figure 1 related to Figure 1.** **a**, Maximum intensity projection of the iris  
892 microvasculature of two-week old mouse, LSFM. Vessels were visualized with IsoB4 (green).  
893 Scale bar, 200  $\mu\text{m}$ ; **b**, the full unprocessed retinal image used for the cropped figure in Fig. 1e.  
894 **c**, P12 retina stained using anti-CD31(Alexa 555), Anti-Erg (alexa488) and anti-Golgi (Golp4,  
895 Alexa 647) imaged using LSFM, Scale bar is 10  $\mu\text{m}$ . **d**, P12 Retina stained for CollagenIV  
896 followed by LSFM imaging. Scale bar is 20  $\mu\text{m}$ . **e**, lifeAct (green) mouse retinas stained for  
897 vessels (IsoB4 - red), merged images shows the overlap between these two channels together  
898 with the plot profile (**g**) of the selected area and the yellow arrow (**f**). **h**, the same channels were  
899 deconvolved using Huygens and **i**, the same area was plotted to compare the image resolution  
900 after deconvolution. Values were normalized to the maximum fluorescence intensity across both  
901 images at each pixel.

902

903 **Supplemental Figure 2 related to Figure 6.** **a**, extended rotational views to see knotted  
904 structure from different angles of tuft 1 and 2 in Fig. 6a taken from movies S14, S15. **b**, 3D  
905 illustration (made with uMake software) while viewing the tuft with curved nuclei (from Fig. 6c  
906 and movie S13) from top to bottom with clipping planes to better understand how the knot  
907 topology changes through the tuft from the vitreous to the plexus side. Blue star indicates the  
908 unexpected vessel joining the top (vitreous facing) surface of the tuft to the plexus below. **c**, a

909 second example of a medium tuft with a swirl structure and clear protrusive sprout-like  
910 morphology to the upper vitreous facing end point of the swirl.

911

## 912 **Movie Legends**

913 **Movie S1.** 3D-rendered LSFM z-stack of retinal eye cups expressing yellow fluorescent protein,  
914 YFP (green) harvest from Thy1-YFP mice and stained with Isolectin IB4 (red).

915 **Movie S2.** 3D-rendered LSFM z-stack of all nuclei (Draq5, magenta) visualizes the inner  
916 nuclear layer and outer nuclear layer of the adult mouse retina. Vessels were visualized by  
917 IsolectinB4 staining (green). The retinal pigment epithelium emits green autofluorescence.

918 **Movie S3.** 3D-rendered LSFM z-stack of an adult mouse retina stained for Tuj1 (green) and  
919 horizontal cells (calbindin, red) visualizing the ganglion cells and horizontal cells, respectively.

920 **Movie S4.** 3D-rendered LSFM z-stack of an adult mouse retina stained for Smooth Muscle Actin  
921 (SMA, red) and CollagenIV staining (CollIV, green) visualizes the three vascular layers and  
922 smooth muscle cells in the mouse retina.

923 **Movie S5.** An hour time lapse LSFM movie showing long, slender filopodia, and rapid “kiss and  
924 run” fusion and disconnection of tip cells at the vascular front of mT/mG x cdh5 (PAC) CreERT2  
925 mice. Frame rate: 1 image/45 sec.

926 **Movie S6.** A 9 hour time lapse LSFM movie showing a connection between two branches in the  
927 capillary plexus of mT/mG x cdh5 (PAC) CreERT2 mice. Frame rate: 1 image/20 min.

928 **Movie S7.** Representative tracking of a short-lived actin-rich bundle in life-Act-EGFP retina mice  
929 imaged with LSFM (7 min). The tracking was performed manually using Manual Tracking plugin  
930 in Fiji/ImageJ.

931 **Movie S8.** Representative tracking of a longer-lived actin-rich bundle in life-Act-EGFP retina  
932 mice imaged with LSFM (30 min). The tracking was performed manually using Manual Tracking  
933 plugin in Fiji/ImageJ.

934 **Movie S9.** Representative tracking of a long-lived actin-rich bundle track in life-Act-EGFP retina  
935 mice imaged with LSFM (40 min). The tracking was performed manually using Manual Tracking  
936 plugin in Fiji/ImageJ.

937 **Movie S10.** 3D-rendered LSFM z-stack of a ‘small tuft’ from an OIR mouse retina stained for  
938 blood vessels (IsolectinB4, green), and the nuclear marker ERG (magenta). The z-stack was  
939 rendered in Imaris.

940 **Movie S11.** 3D-rendered LSFM z-stack of a ‘medium tuft’ from an OIR mouse retina stained for  
941 blood vessels (IsolectinB4, green), and the nuclear marker ERG (magenta). The z-stack was  
942 rendered in Imaris.

943 **Movie S12.** 3D-rendered LSFM z-stack of a ‘large tuft’ from an OIR mouse retina stained for  
944 blood vessels (IsolectinB4, green), and the nuclear marker ERG (magenta). The z-stack was  
945 rendered in Imaris.

946 **Movie S13.** 3D-rendered z-stack showed a curved nuclei in a ‘medium tuft’ from an OIR mouse  
947 retina stained for blood vessels (IsolectinB4, green), and the nuclear marker ERG (magenta).  
948 The z-stack was rendered in Imaris.

949 **Movie S14.** 3D-rendered LSFM z-stack deconvolved in Huygens then reconstructed with  
950 surface rendering in Imaris of ‘Large tuft 1’ from an OIR mouse retina stained for blood vessels  
951 (IsolectinB4, green), and the nuclear marker ERG (red).

952 **Movie S15.** 3D-rendered LSFM z-stack deconvolved in Huygens then reconstructed with  
953 surface rendering in Imaris of ‘Large tuft 2’ from an OIR mouse retina stained for blood vessels  
954 (IsolectinB4, green), and the nuclear marker ERG (red).

955 **Movie S16.** 3D-rendered LSFM z-stack deconvolved in Huygens then reconstructed with  
956 surface rendering in Imaris of a ‘small tuft’ from an OIR mouse retina stained for blood vessels  
957 (IsolectinB4, green), and the nuclear marker ERG (red).

958 **Movie S17.** 3D-rendered LSFM z-stack deconvolved in Huygens then reconstructed with  
959 surface rendering in Imaris of 'a Medium swirl tuft' from an OIR mouse retina stained for blood  
960 vessels (IsolectinB4, green), and the nuclear marker ERG (red).

961 **Movie S18.** A 2.5 hour time lapse movie of a retinal tuft of a mouse in the OIR model using  
962 mT/mG x cdh5 (PAC) CreERT2 mice visualize short, rapidly extending and retracting filopodia  
963 as compared to control retinas. Frame rate: 1 image/minute.

964 **Movie S19.** A 2.5 hour time lapse movie of mouse retinal vasculature in the OIR model using  
965 mT/mG x cdh5 (PAC) CreERT2 mice reveal cell shuffling in real-time. Frame rate: 1  
966 image/minute.

967 **Movie S20.** A 2.5 hour time lapse movie of mouse retinal vasculature in the OIR model using  
968 mT/mG x cdh5 (PAC) CreERT2 mice reveal abnormal vessel growth in real-time. Frame rate: 1  
969 image/minute.

970

**Figure 1.**

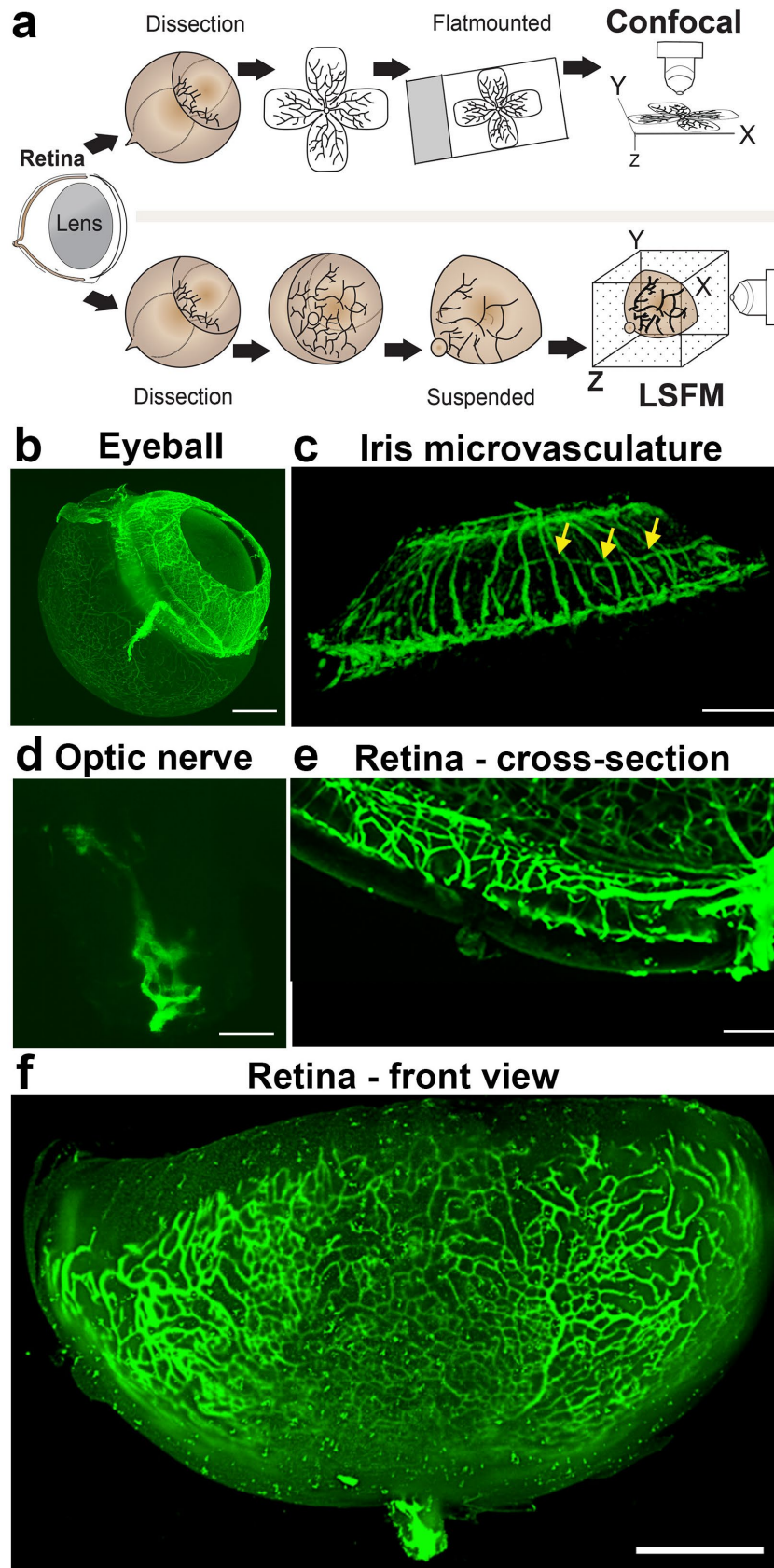




**Figure 2.**

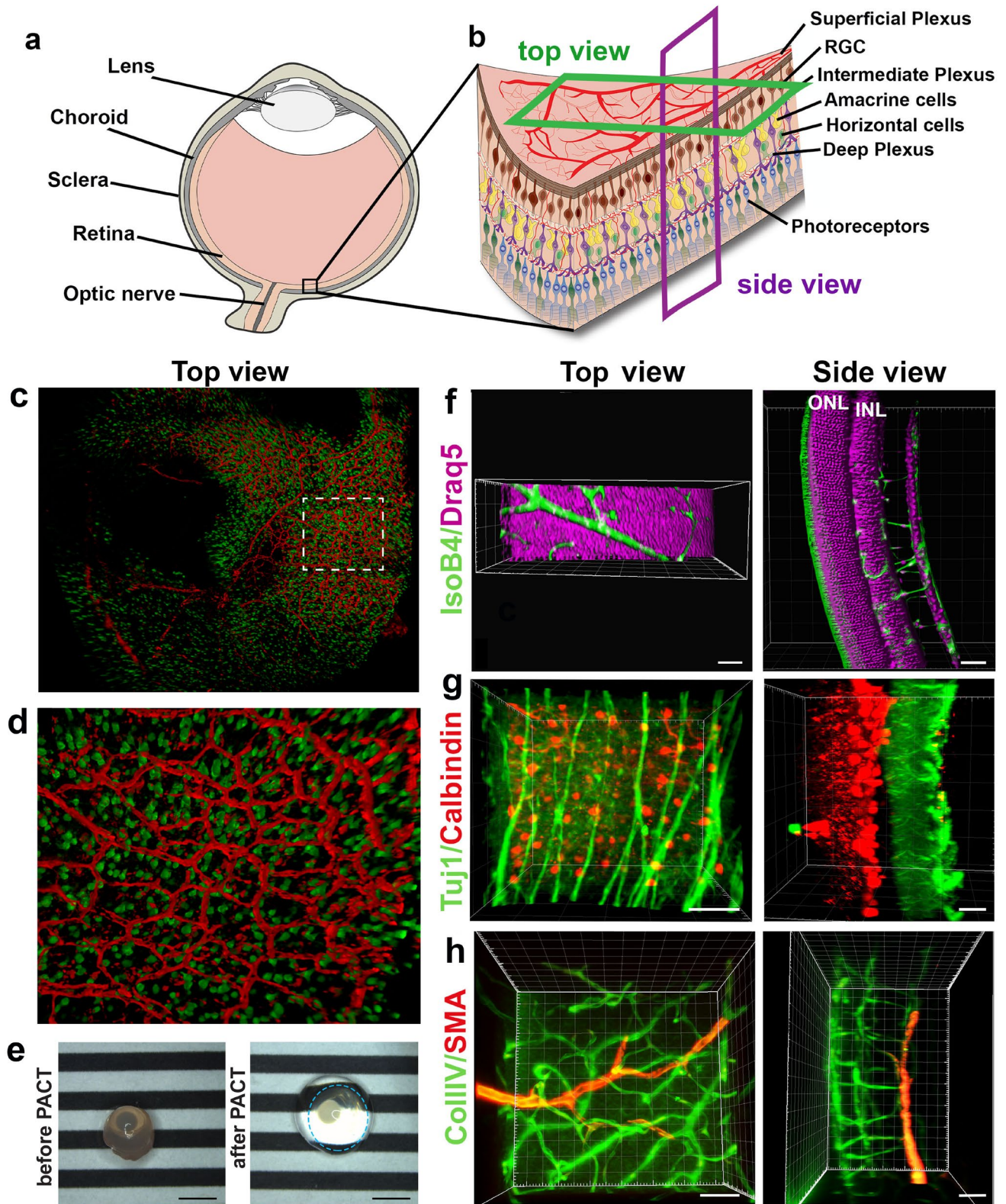


### Figure 3.

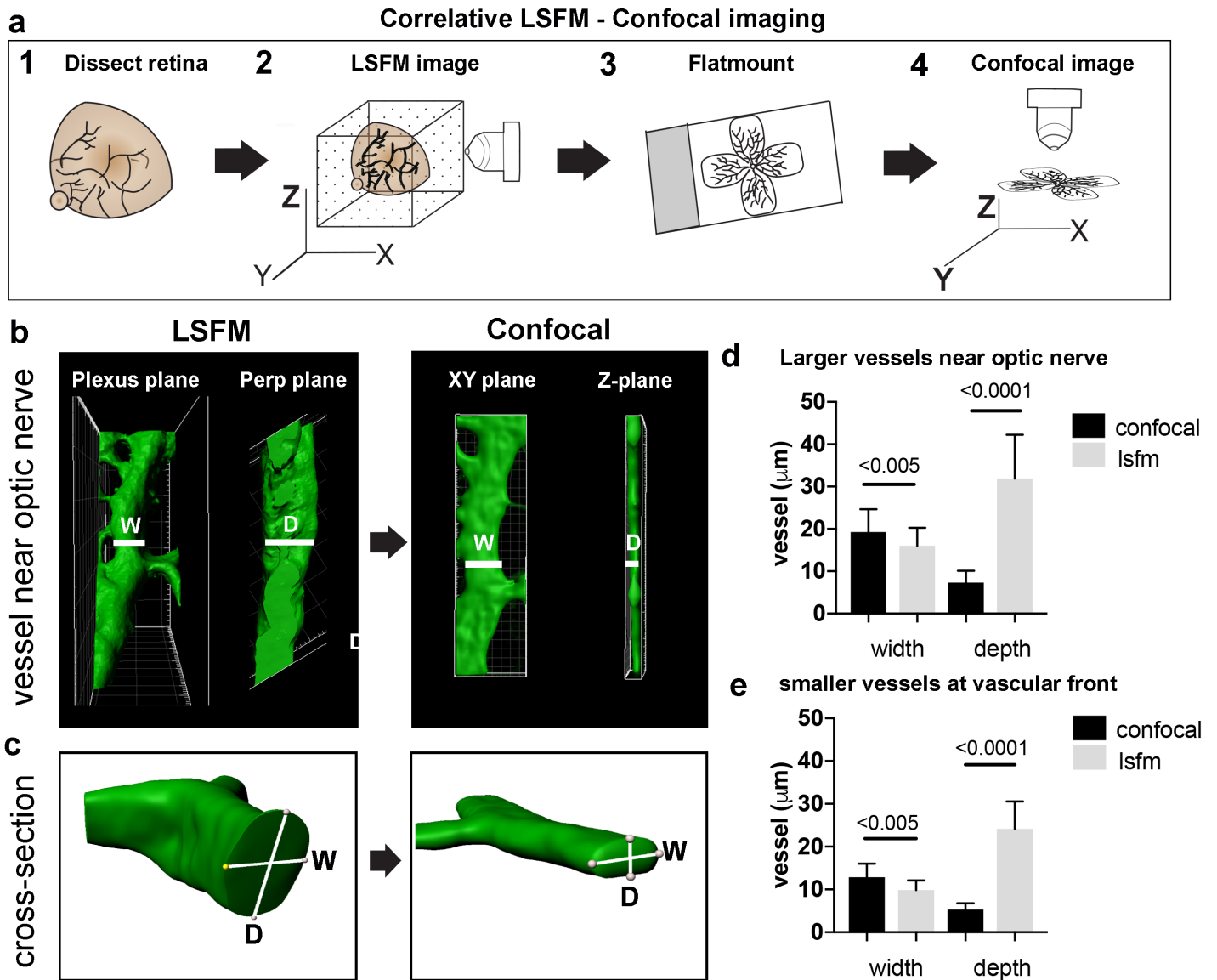




## Figure 4.

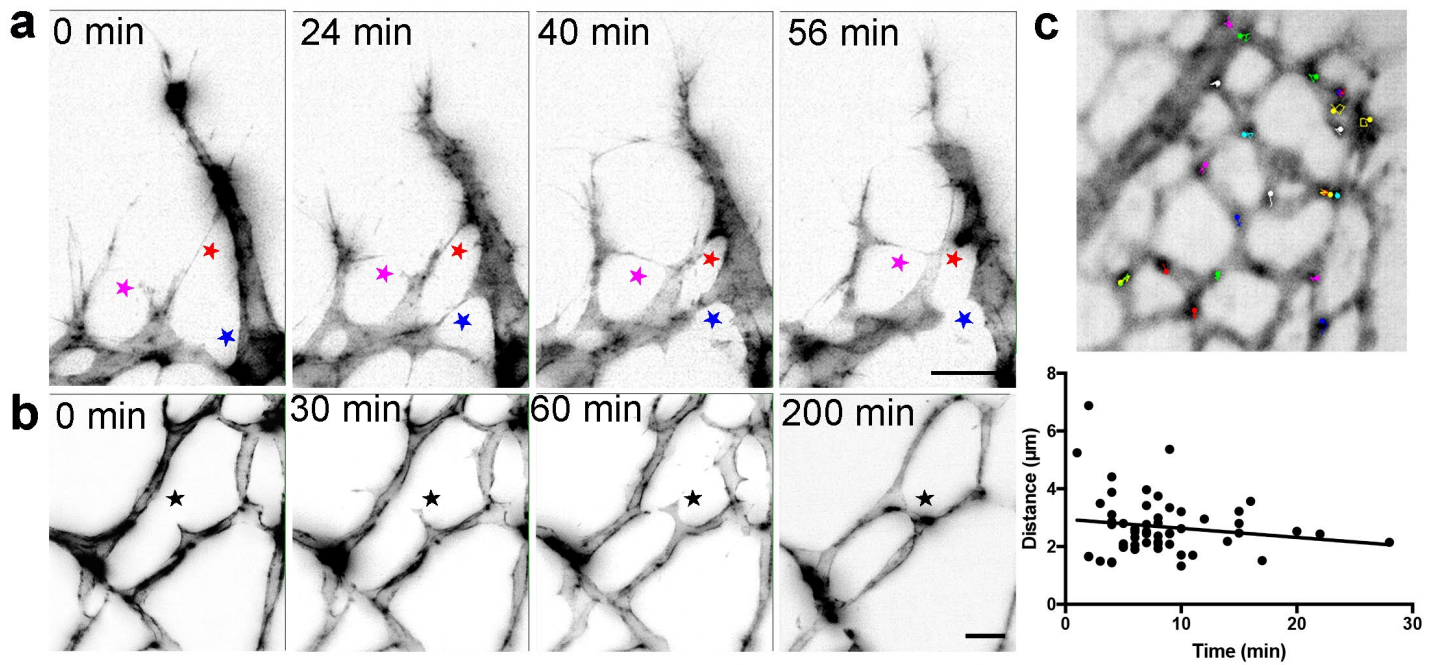


## Figure 5.

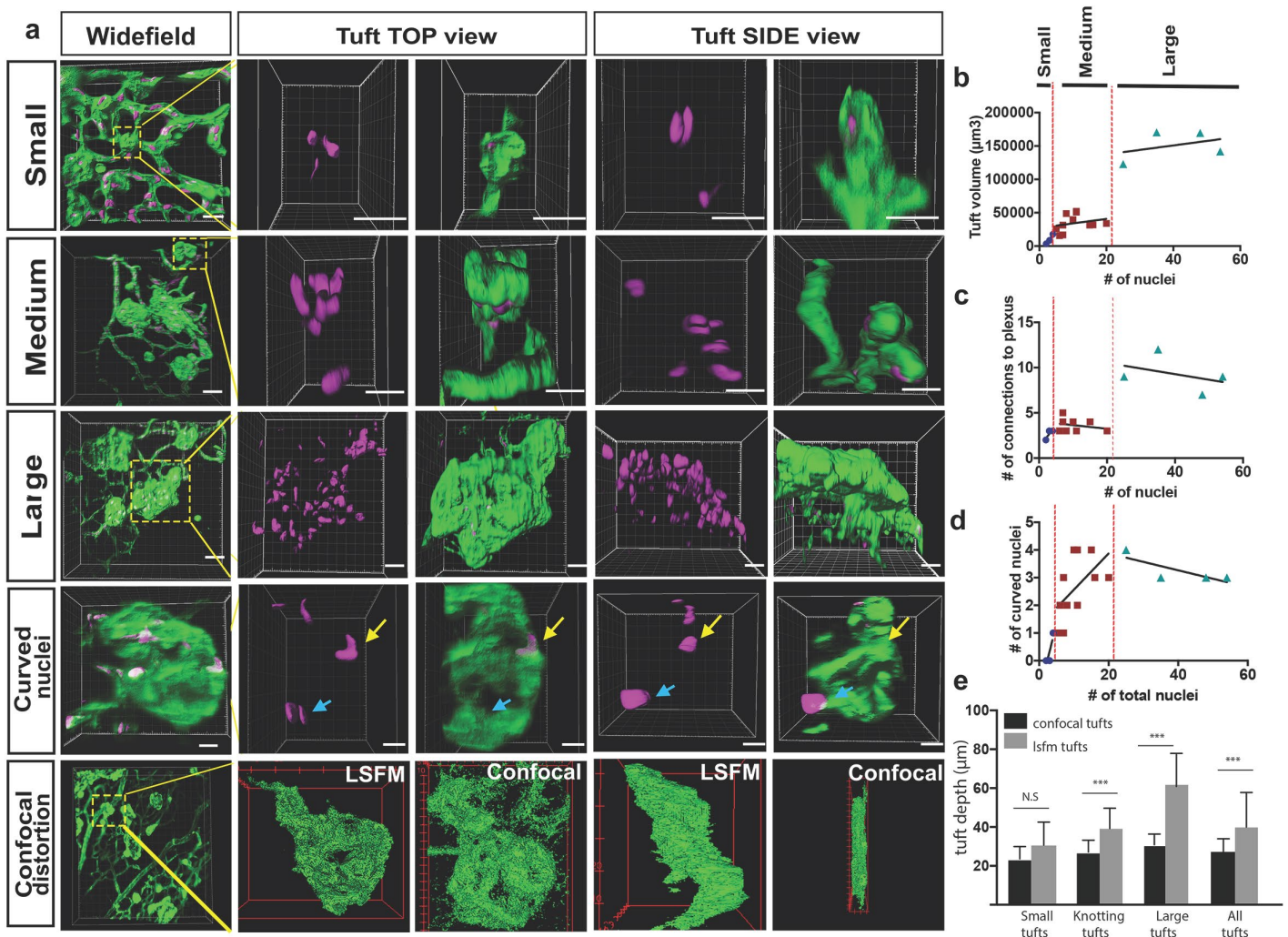


## Figure 6.

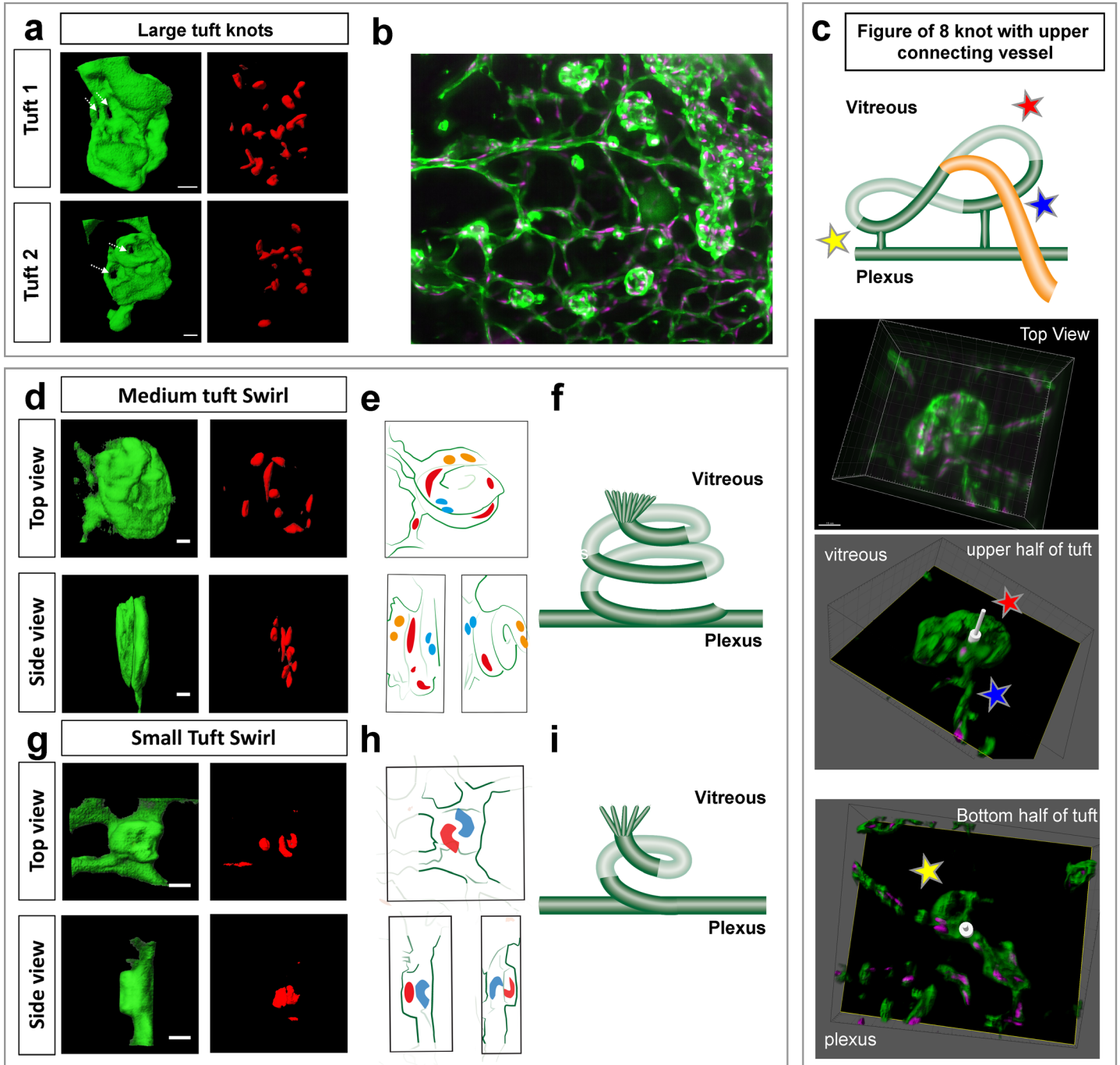
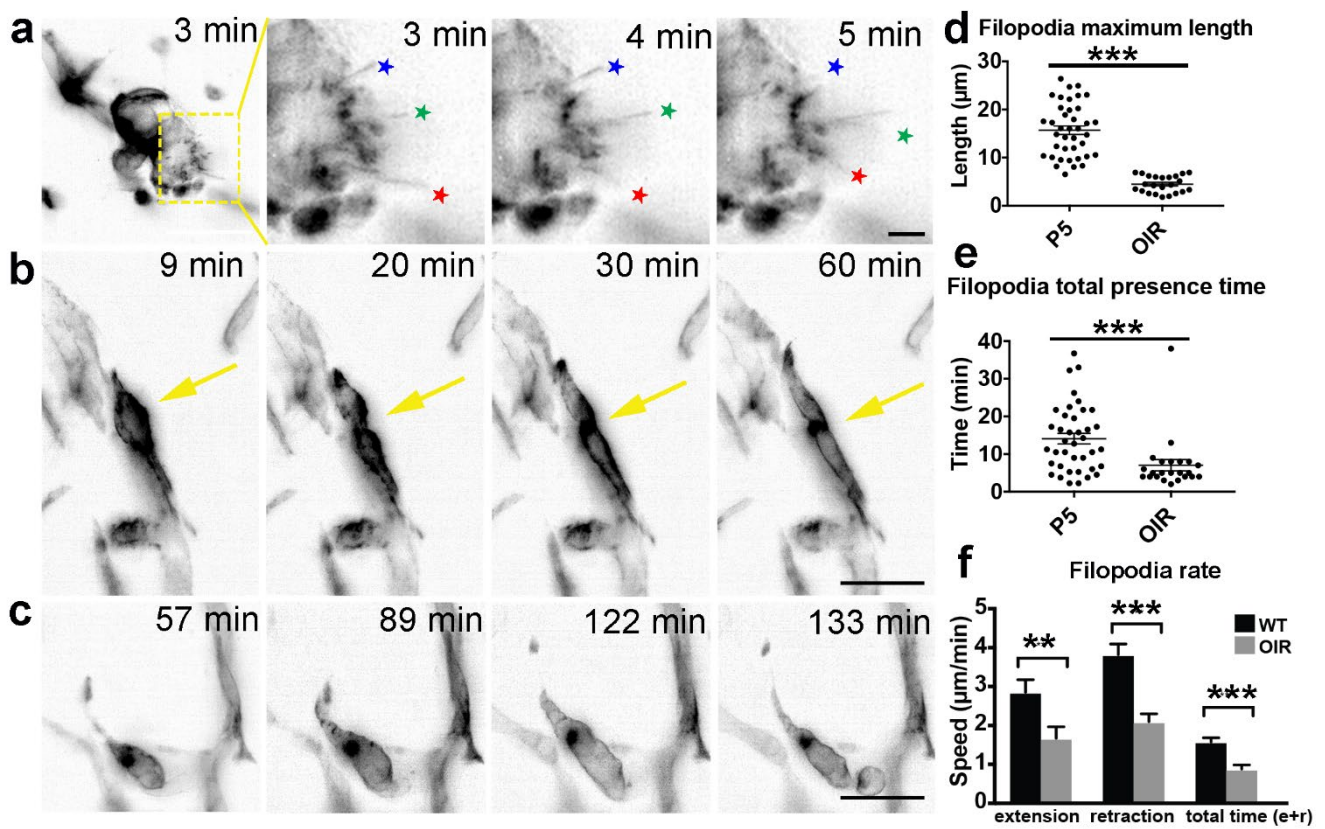
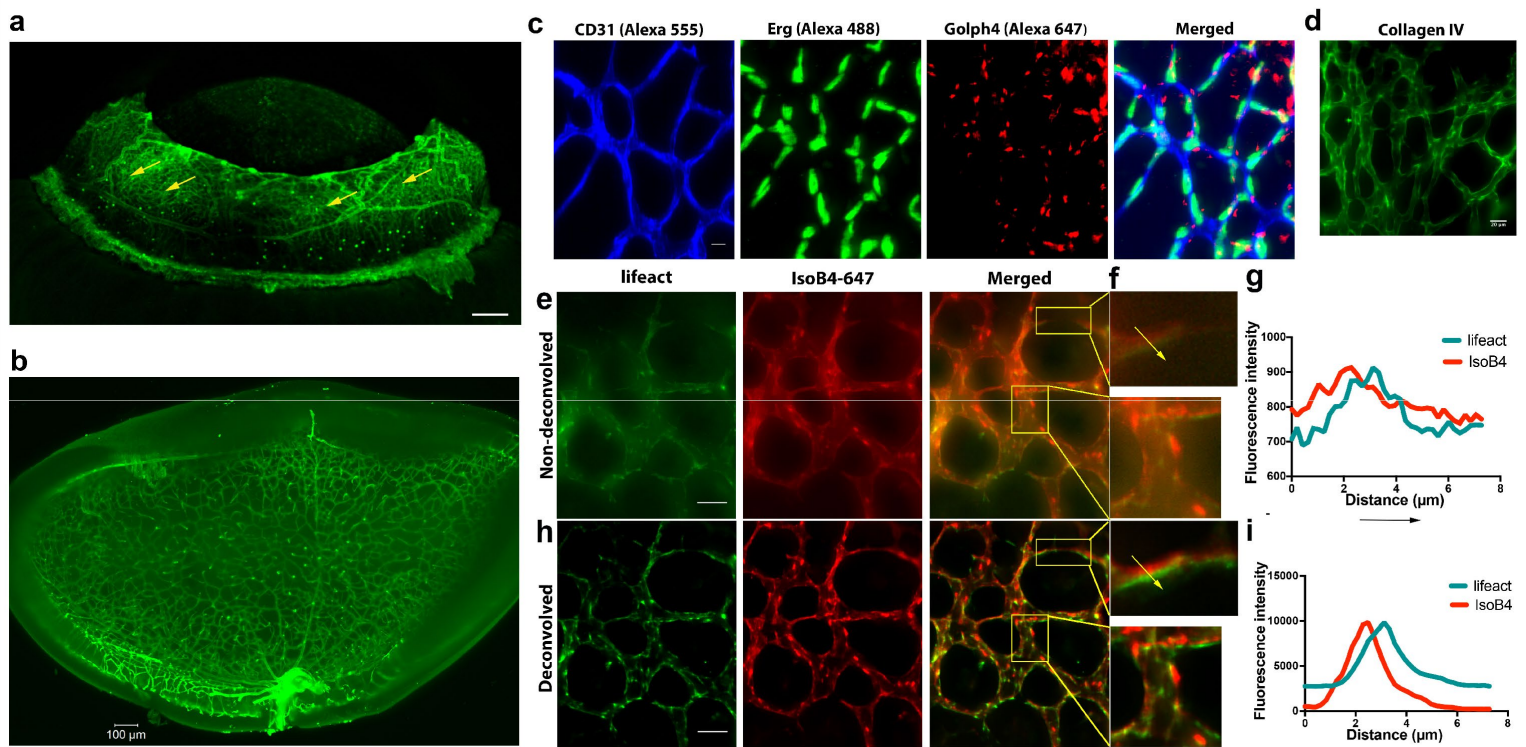


## Figure 7.





## Supp. Figure 1.



## Supp. Figure 2.

